Chemical Engineering Science 191 (2018) 169–182

Contents lists available at ScienceDirect

Chemical Engineering Science

journal homepage: www.elsevier.com/locate/ces

Mechanistic insights into the direct propylene epoxidation using Au nanoparticles dispersed on TiO_2/SiO_2

Jingjing Ji [a], Zheng Lu [b], Yu Lei [b], C. Heath Turner [a],*

[a] *Department of Chemical and Biological Engineering, The University of Alabama, Tuscaloosa, AL 35487, United States*
[b] *Department of Chemical and Materials Engineering, The University of Alabama in Huntsville, Huntsville, AL 35899, United States*

HIGHLIGHTS

- KMC simulations probe the direct propylene oxide reaction mechanism and associated byproducts.
- Propylene oxide selectivity can be enhanced by decreasing temperature and increasing H_2/C_3H_6.
- The synergistic role of Au/Ti dual interface sites is emphasized in the product formation.
- Formation of side products is correlated with the surface coverage of atomic oxygen on Au particles.

GRAPHICAL ABSTRACT

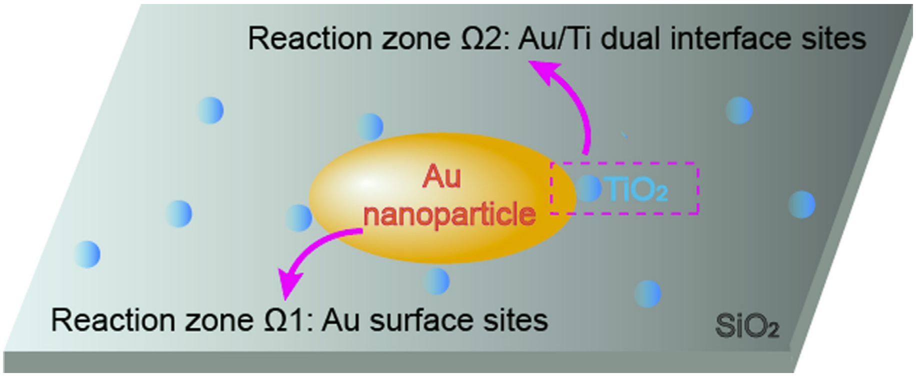

ARTICLE INFO

Article history:
Received 24 March 2018
Received in revised form 6 June 2018
Accepted 24 June 2018
Available online 25 June 2018

Keywords:
Propylene epoxidation
Kinetic Monte Carlo (KMC)
Reaction mechanism
Au/Ti dual interface sites
Heterogeneous catalysis

ABSTRACT

Direct propylene epoxidation is an important gas-phase reaction for the future industrial production of propylene oxide (PO). However, the mechanistic understanding of this reaction system is still elusive, including the role of side reactions. Herein, kinetic Monte Carlo (KMC) simulations are applied to explore the underlying mechanistic aspects of propylene epoxidation over $Au/TiO_2/SiO_2$, and consistent results are obtained with respect to experimental benchmarks. The present study systematically probes the reaction mechanism, which involves acrolein formation on Au nanoparticles as well as the formation of PO and several byproducts at the Au/Ti dual interface sites, and it highlights the synergistic effect of interface sites in heterogeneous catalysis. The origin of the negative effect of rising reaction temperature on PO selectivity has been clarified, as it is correlated with decreasing atomic oxygen coverage on the Au surface. The varying feed concentration of $H_2/O_2/C_3H_6$ leads to different coverages on the catalyst surface, emphasizing the importance of an optimum H_2/C_3H_6 inlet concentration ratio for enhancing PO selectivity and hydrogen utilization efficiency. Based on our model results, we propose that supports with acidic groups may promote hydroperoxy species transferring to the adjacent Ti sites, thereby decreasing its decomposition to atomic oxygen on the Au sites, which leads to byproduct formation.

1. Introduction

Coinage metal gold was previously regarded as a catalytically inert material. This common assumption was dramatically shifted by the discovery of low-temperature CO oxidation with

---

* Corresponding author.
E-mail address: hturner@eng.ua.edu (C.H. Turner).

https://doi.org/10.1016/j.ces.2018.06.064
0009-2509/

metal oxide supported gold nanoparticles in 1987 (Masatake et al., 1987). Since that time, supported Au nanoparticles have attracted wide research interest in the field of heterogeneous catalysis, such as chemoselective hydrogenation (Corma and Serna, 2006), water-gas shift (Fu et al., 2003; Rodriguez et al., 2007), the selective oxidation of olefins (Hughes et al., 2005; Turner et al., 2008), etc. Herein, olefin oxidation, in particular propylene (C_3H_6) epoxidation to produce propylene oxide (PO), has attracted considerable attention since PO is a key intermediate for the industrial production of polyether polyols, propene glycols, and propene glycol ethers (Huang and Haruta, 2012), which are mainly used to manufacture commercial products such as foams, adhesives, and solvents (Nijhuis et al., 2006; Yap et al., 2004). Unfortunately, the current chlorohydrin process to produce PO suffers from environmental issues, and the hydroperoxide process is challenged by poor economics and the formation of byproducts. In contrast, the direct vapor-phase propylene epoxidation with molecular H_2 and O_2 catalyzed by nano-sized Au deposited on TiO_2 has been proved to be clean and highly selective. This route was first discovered by Haruta and co-workers in 1998 (Hayashi et al., 1998).

Over the past 20 years, a lot of experimental and theoretical efforts have been dedicated to improving Au-based catalysts and understanding the fundamental reaction features of direct propylene epoxidation (Chen et al., 2013a; Chen et al., 2013b; Joshi et al., 2006, 2007b; Lee et al., 2012; Nijhuis et al., 1999; Nijhuis et al., 2006; Pulido et al., 2012; Stangland et al., 2000; Wells et al., 2004a). In this system, the active oxygen species, hydrogen peroxide (H_2O_2), is readily synthesized on the anchored Au nanoparticles, and it subsequently migrates to the adjacent Ti sites to convert propylene into PO. The H_2O_2 formation via H_2 and O_2 has been investigated on a number of different surfaces, from Au particles (Barton and Podkolzin, 2005; Joshi et al., 2007a; Landon et al., 2002; Wells et al., 2004b) to other transition metal surfaces (Ni, Pd, Pt, Cu, Ag, and Rh) (Düzenli et al., 2015; Ford et al., 2010; Freakley et al., 2016; Landon et al., 2003). Despite a rising interest, the mechanistic comprehension of direct propylene epoxidation is still under intense debate. There are several controversial issues: (i) the main factors that affect the catalytic activity of nanoscale Au; (ii) the origin of the activated oxidant (Ti–OOH), and the sites that are responsible for the direct PO reaction; and (iii) the mechanistic aspects of side reactions, as well as their influence on PO selectivity and catalyst deactivation.

It is commonly believed that size and morphology are significant parameters for the catalytic activity of Au nanoparticles. For instance, estimates of the optimal Au nanoparticle size for propylene epoxidation, have reduced from 2 to 5 nm in the early studies of Haruta and Daté (2001) and Hayashi et al. (1998) to sizes smaller than 2 nm in diameter (Huang and Haruta, 2012; Huang et al., 2010; Okumura et al., 2015). In contrast, both density functional theory (DFT) calculations and indirect experimental evidence have suggested that tiny Au clusters (composed of a few atoms) incorporated in microporous channels ($\sim$0.55 nm) of TS-1 could be responsible for the high activity (Huang and Haruta, 2012; Joshi et al., 2006, 2007b; Lee et al., 2012; Yap et al., 2004). The activity of Au nanoparticles has been ascribed to quantum size effects (Valden et al., 1998), high step-density and strain on Au nanoparticles (Mavrikakis et al., 2000), and charge-transfer due to electronic interactions between particles and oxide supports (Yoon et al., 2005). However, H_2 dissociation experiments have revealed that the most active sites are gold atoms in contact with the TiO_2 support, which further support the hypothesis that the Au/support interface is crucial for the formation of active sites (Fujitani et al., 2009). In short, the unusual activity of nanometer-sized Au particles is still an open question, and no consensus has been reached to date.

Hydrogen peroxide formation on Au nanoparticles is viewed as a key reaction step prior to its spillover onto a TiO_2 support, leading to the formation of metal peroxo compounds (Ti–OOH species) (Bravo-Suárez et al., 2008; Hayashi et al., 1998; Uphade et al., 2002; Wells et al., 2004a). Theoretical calculations have predicted the existence of H_2O_2 on Au particles (Olivera et al., 1994; Wells et al., 2004a,b), whereas experimental verification has been challenging, since H_2O_2 is unstable and easily decomposes into water at high temperature (Lee et al., 2012). Thus, whether H_2O_2 is just a spectator or a reactive species is obscured. Even though the H_2O_2 intermediate is known to be an active species, its lifetime on an Au/TiO_2 surface is unknown, and it may degrade before reaching the Ti sites. Recently, an inelastic neutron scattering (INS) study (Sivadinarayana et al., 2004) and an in situ UV spectroscopy study (Chowdhury et al., 2006) offered direct spectroscopic evidence for the formation of H_2O_2 and the hydroperoxy radical (OOH) species, originating from H_2-O_2 related reactions over Au/TiO_2. Furthermore, both experimental and theoretical studies regarding the propylene epoxidation with a mixture of O_2/H_2O indicated that, instead of H_2O_2, it is the OOH radical ($O_2^* + H_2O^* \leftrightharpoons OOH^* + OH^*$, where $*$ stands for the adsorbed species) that directly migrates to the neighboring Ti site to form Ti–OOH species, resulting in PO production (Chang et al., 2015; Chang et al., 2011; Liu et al., 2016; Ojeda and Iglesia, 2009). Nonetheless, the active oxidizing species is still unverified (OOH^* or $H_2O_2^*$) due to the absence of transient kinetic data. In addition, there are different opinions about the active sites for the epoxidation reaction. A reasonable proximity between Au and Ti sites is generally considered to be indispensable for the PO reaction, suggesting the existence of a well-defined reaction zone (Driscoll et al., 2017; Fujitani et al., 2009; Joshi et al., 2007b; Lee et al., 2012; Panayotov et al., 2016; Taylor et al., 2006; Yap et al., 2004). However, several DFT studies have suggested that single gold particles can catalyze propylene epoxidation without the participation of Ti sites (Joshi et al., 2006; Moskaleva, 2016).

Gold-titania systems are able to catalyze propylene epoxidation with a mixture of H_2/O_2 under very mild conditions (atmospheric pressure and 323–393 K) and exhibit high PO selectivity (>99%) (Nijhuis et al., 2005b; Stangland et al., 2000). Despite the high selectivity of the gold-titania catalysts, the propylene conversion is typically low (<2%) and the hydrogen efficiency (<30%) is insufficient (Nijhuis et al., 2005b; Zwijnenburg et al., 2004). Attempts to improve propylene conversion by raising the reaction temperature, inevitably lead to decreasing PO selectivity due to consecutive PO reactions (isomerization, oligomerization, and oxidative cracking) (McEntee et al., 2015; Moskaleva, 2016; Okumura et al., 2015; Stangland et al., 2000; Uphade et al., 2002). These secondary reactions generate byproducts such as propanal, acetone, ethanal, CO_2, dioxane, and acids. It is worth noting that acrolein is another significant byproduct (Stangland et al., 2000). The allylic hydrogen of propylene is acidic and labile, and easily suffers from the nucleophilic attack of the oxygen radicals bound to Au nanoparticles, since the oxygen species behave as a Brønsted base (Baker et al., 2011; Dai et al., 2017; Wells et al., 2004a; Yap et al., 2004). Friend and Moskaleva have identified acrolein formation on the Au surface, but with different intermediates (Deng et al., 2006; Liu and Friend, 2010; Moskaleva, 2016). Additionally, in situ fourier transform transmission infrared spectroscopy (FTIR) combined with DFT calculations highlighted the ketenylidene ($Au_2C{=}C{=}O$) formation from propionic and acetic acids at the Au/TiO_2 perimeter sites (Green et al., 2012; McEntee et al., 2015). Nevertheless, detailed information with respect to side reaction pathways is limited, which limits our ability to suppress undesired byproduct formation.

In this work, kinetic Monte Carlo (KMC) simulations are performed to simulate the chemical kinetics of direct propylene epoxidation. This spatially-resolved modeling approach can narrow the gap between DFT studies and experimental efforts, due to its ability to connect variations in the atomistic and electronic structure of a catalytic surface with its activity and selectivity. Until now, little effort has been made to establish a complete reaction network or assess a reliable kinetic model with relevant side reaction channels encountered at typical reaction conditions (Chen et al., 2011; Stangland et al., 2000). Previous kinetic experiments have been carried out to obtain relevant elementary reaction steps and rate expressions, whereas mechanistic information derived from these kinetic tests has been limited (Barton and Podkolzin, 2005; Bravo-Suárez et al., 2008; Bravo-Suárez et al., 2007; Perez Ferrandez et al., 2015). Our previous KMC studies (Turner et al., 2017) have probed the effect of different reaction conditions on PO formation rates, but they neglected to take into account relevant byproducts and the corresponding reaction pathways. Motivated by the need for a more comprehensive mechanism, in this work, we show that KMC simulations in combination with experimental benchmarking provide valuable insight into the impact of reaction conditions (temperature, reactant concentration) on PO selectivity, hydrogen efficiency, and catalyst activity. This allows us to qualitatively describe the PO reaction mechanism, including side product involvement, and it allows us to pose a strategy for enhancing the catalyst activity.

2. Simulation methods

2.1. The model and reaction fundamentals

KMC simulations are able to explicitly track the spatial and temporal evolution behavior of all surface intermediates, and have been previously invoked to model catalytic and other activated processes (Hess and Over, 2017; Hess et al., 2017; Hu et al., 2009a,b; Mei et al., 2010; Mei et al., 2009; Mei et al., 2006; Turner et al., 2016; Zheng et al., 2008). A summary of the events (adsorption, desorption, diffusion, and surface reaction) in the present catalytic system and their activation energies have been expanded from our previous investigation (Turner et al., 2017), and this updated database is included as Table S1 in the Supporting Information. The active barrier parameters are based on DFT studies and experimental reports in the literature. For each forward elementary step, its reverse reaction and the corresponding active barrier are taken into consideration to fulfill the detailed-balance criterion. The active barrier database in Table S1 is used to compute the event rates. The reaction rate constant k_i of each elementary reaction, diffusion, and desorption step is calculated using transition state theory as shown in Eq. (1) (with $\upsilon_i = k_BT/h$). While k_i for each adsorption process on vacant sites is evaluated with the kinetic theory of gases, according to Eq. (2).

$$k_i = \upsilon_i \cdot \exp\left(\frac{-\Delta E_{a,i}}{RT}\right) \tag{1}$$

$$k_{ads,i} = \frac{s_0 \cdot P_i \cdot A_s}{\sqrt{2\pi \cdot MW_i \cdot RT}} \cdot \exp\left(\frac{-\Delta E_{a,i}}{RT}\right) \tag{2}$$

In Eqs. (1) and (2), $\Delta E_{a,i}$ is activation barrier, h is Plank's constant, k_B is Boltzmann's constant, P_i is the partial pressure of species i, R is the gas constant, MW_i is the molecular weight of species i, A_s is the area of the adsorption site (corresponding to the area of an individual grid cell), and s_0 is the sticking coefficient (assumed to be unity for all species).

In our KMC simulations, the experimental catalyst surface ($Au/TiO_2/SiO_2$) is mapped to a periodic lattice consisting of a two-dimensional (2-D) array, with a nominal size of 200 × 200. The justification of our simulation model has been described in our previous investigation (Turner et al., 2017). The initial SiO_2 surface is decorated with Ti sites, as well as Au nanoparticles (represented by 2-D discs on the surface grid). In the KMC model, the diameter of Au nanoparticles ranges from 1 to 6 nm on the basis of a random distribution, consistent with an average particle size of 2.1 nm observed in the experimental benchmark system (Lu et al., 2018). The experimental Au loading is approximately 0.06 wt% which is used to make quantitative rate comparisons (on a per Au mass basis) between the simulations and experiments. Although the exact size of Au nanoparticles in each KMC simulation varies, the results are always normalized regarding the gold mass in each simulation run, in order to make consistent comparisons with experiments. The coverage (concentration) of Ti sites in the model is set at 10% which corresponds to the estimated 9.7% concentration on the experimental surface. All Ti sites are randomly distributed on the SiO_2 surface by directly replacing the surface Si sites. A snapshot of the basic model layout is shown in Fig. 1. These grid sites can either be vacant or occupied by various surface reactive species during KMC simulations, and neighbor-neighbor interactions are currently excluded.

The reaction cycle proceeds by the adsorption of hydrogen, oxygen, and propylene. H_2^* ($*$ represents an Au surface-bound species) dissociation into $2H^*$, requires two neighboring empty Au surface sites, while the direct O_2^* dissociation was estimated to be less favorable on Au nanoparticles (Barton and Podkolzin, 2005; Chang et al., 2015; Chang et al., 2011; Kettemann et al., 2017). Instead, atomistic hydrogen H^* can react with O_2^* to generate OOH^* which can further react to form $H_2O_2^*$. The $H_2O_2^*$ (OOH^*) species is labile, and it can either directly degrade into water (Scheme 1) or readily decompose to hydroxyl groups that react with H^* to produce water (Table S1). Consequently, atomistic O^* is co-produced along with $H_2O_2^*$ or OOH^* decomposition. All these H_2-O_2 related reactions exclusively proceed on the surface sites of Au nanoparticles, referred to as reaction zone Ω1 in Fig. 2.

The degradation of $H_2O_2^*$ contributes to a large amount of water production, versus the stoichiometric epoxidation reaction (Chen et al., 2011). It is debated whether it is OOH^* generated on Au nanoparticles that directly transfers to the adjacent Ti site to form Ti–OOH species, or if $H_2O_2^*$ first travels to the neighboring Ti site and in turn forms Ti–OOH via dissociation. In our present simulation, we assume OOH^* spillover onto the adjacent Ti sites leading to the Ti–OOH intermediate, based on chemical intuition and previous literature reports (Chang et al., 2011; Chowdhury et al., 2006;

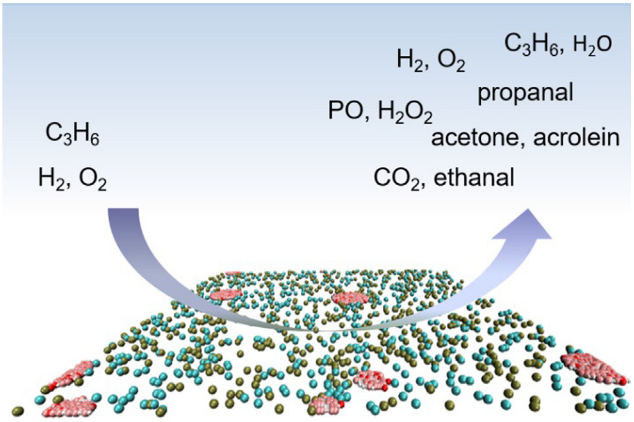

Fig. 1. Illustration of the KMC model system. The two-dimensional periodic catalyst surface is coupled to the gas phase composition via adsorption/desorption steps. On the surface, the red/pink/white sites correspond to different species on the Au nanoparticles, while the cyan/olive sites correspond to different species on the TiO_2/SiO_2 surface. (For interpretation of the references to colour in this figure legend, the reader is referred to the web version of this article.)

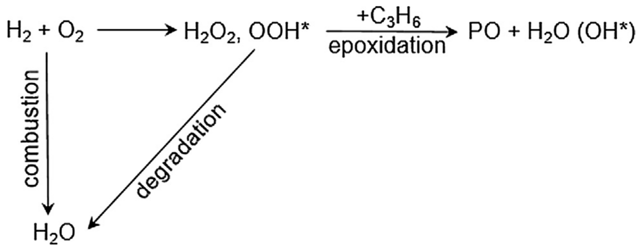

Scheme 1. Simplified scheme for H_2O formation over $Au/TiO_2/SiO_2$.

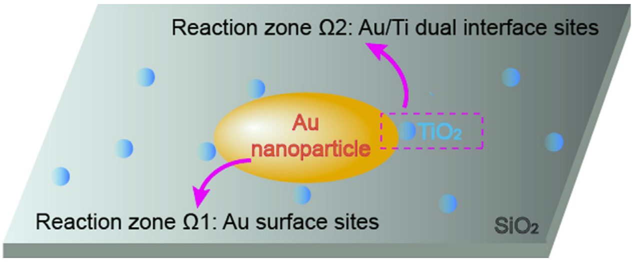

Fig. 2. Graphical representation of different reaction zones for catalyst $Au/TiO_2/SiO_2$. Yellow, blue, and gray colors indicate Au nanoparticles, TiO_2 sites, and SiO_2 support, respectively. Reaction zone Ω1: reactions occur on the surface sites of Au nanoparticles. Reaction zone Ω2: reactions occur on the Au/Ti dual interface sites, in which one Ti site is in direct contact with one or several Au sites. (For interpretation of the references to colour in this figure legend, the reader is referred to the web version of this article.)

Ojeda and Iglesia, 2009; Sivadinarayana et al., 2004). Previously experiments indicated that perimeters between Au particles and Ti sites are active for the epoxidation reaction (Haruta, 1997; Haruta and Daté, 2001), and several side reactions (isomerization and oxidative cracking, etc.) occur at the gold-titania interface (Nijhuis et al., 2005b; Stangland et al., 2000). As a consequence, the PO reaction and side reactions are allowed to proceed at the Au/Ti dual interface sites as shown in the reaction zone Ω2 of Fig. 2. The reaction zone Ω2 is formed by the direct contact between a Ti site and at least one Au nanoparticle site. This type of reaction mechanism can be efficiently captured with KMC simulations, since it can account for the spatial and temporal distribution of surface reaction intermediates on the catalyst, important for fully capturing the experimental aspects.

2.2. KMC simulation approach

Using a pre-specified database of system events and rate information, the system is moved forward through time by implementing the variable time step KMC algorithm, where there is only one event per time step but for each event the time step size can vary. Starting from the initial system configuration, the rates for all events are summed together to calculate the total rate, $\sum r_i$. After that, the system clock is then advanced according to Eq. (3), where Δt is the variable time step for the next event to occur and RN is a random number, evenly distributed between 0 and 1. The total reaction time of the system is accordingly updated by adding the computed Δt to the current time.

$$\Delta t = \frac{-\ln(RN)}{\sum r_i} \tag{3}$$

After the clock has been incremented, the system configuration is then updated by stochastically selecting an event to occur. The specific event that occurs within each time step is chosen according to Eq. (4), which takes into account the relative probability of each step.

$$P_i = \frac{r_i}{\sum r_i} \tag{4}$$

After updating the configuration of the system, the procedure above is repeated over and over again so that the system experiences a spatiotemporal evolution through stepping in kinetic events, thereby updating the gas phase products as well as surface species and compositions. This enables us to calculate turnover frequencies (TOFs), surface coverages, reaction rates and other average properties.

In order to evaluate the reproducibility of the KMC results, five different independent simulations are conducted at each condition, and each simulation is propagated through time for a minimal duration of 400×10^6 KMC steps, ensuring adequate sampling. These independent simulations allow for statistical fluctuations of the numerical values, but each simulation also corresponds to a slightly different surface configuration (Au nanoparticle sizes are chosen from a random distribution mentioned before, their positions on SiO_2 surface are randomly assigned, and the Ti site positions also vary). As the simulation proceeds, the catalyst structure remains fixed, but the species on the surface can adsorb, desorb, react and diffuse.

A unique characteristic of our KMC simulations is the coupling between the surface adsorption/desorption steps and the bulk gas phase composition (as described in our previous work (Turner et al., 2017)), which allows for the product species to potentially re-adsorb onto the catalyst surface. This coupling behavior also allows us to track the variation in the gas concentration and composition as the reaction proceeds. After obtaining equilibrium, the selectivity is calculated (Eqs. (1)–(6) in Supporting Information), with the volume of the bulk gas phase above the catalyst surface and the total pressure (1 bar) fixed for each reaction condition.

One important challenge in our KMC simulations is the problem of stiffness due to the existence of disparate time separation in this catalytic reaction network. For instance, fast reaction channels (like diffusion, with low activation barriers) typically occur much more frequently and will statistically dominate the moves performed in the simulation. In contrast, slow processes (like surface reactions, with high activation barriers) may have rates so low that they are not adequately sampled during a typical simulation. In our case, both PO and byproduct formation at the Au/Ti perimeter interface are slow processes in comparison with H_2-O_2 related reactions as well as diffusion steps on Au nanoparticles, whereas the former are the reactions of interest and crucial for evaluating the product selectivity. Thus, adequate sampling of the slow reactions is critical. Some efforts to resolve the stiffness have been made in previous simulations of chemical kinetic systems by treating the fast or slow reactions with different approximations (Dybeck et al., 2017; Haseltine and Rawlings, 2002; Janssen, 1989a,b; Rao and Arkin, 2003; Samant and Vlachos, 2005).

According to our previous work, we artificially lower the activation barrier of the rate-determining step for PO and byproduct formation, in order to improve sampling of the slow steps, and then we apply a simple scaling relationship to extrapolate the simulation results to correspond to the full activation barrier value. Preliminary tests were performed to check for any unintended deviations in other quantities (surface coverages of individual species, adsorption/desorption rates, etc.).

3. Reaction network

When referring to the olefin epoxidation process, the most commonly used mechanism is the formation of oxametallyacycle intermediates. For example, the ethylene epoxidation on Ag(1 1 1) to produce the ethylene oxide (EO) is considered to undergo an oxametallacycle, namely, OMME (oxygen-metal-metal-ethylene, a five-member ring) or OME (oxygen-metal-ethylene, a four-member ring) complex (Bocquet and Loffreda, 2005; Mavrikakis et al., 1998; Torres et al., 2005). These oxametallacycle complexes have been experimentally identified on the silver surface (Jones et al., 1998; Linic and Barteau, 2002; Linic et al., 2002). The OME complex with a single Ag atom in its ring is suggested to be much more selective toward EO formation. In contrast, the OMME intermediate with two Ag atoms incorporated preferably supports the acetaldehyde production (Özbek and van Santen, 2013).

Recently, Moskaleva (2016) displayed a two-step reaction mechanism for PO formation using OOH* on an Au(3 2 1) surface via an OMP (oxygen-metal-propylene, a four-member ring) complex, in which: (1) an OMP intermediate formed first with one C—O (the carbon is either one of C=C) bond formation; and then (2) the Au—C bond is cleaved to form a three-membered ring, PO. This two-step reaction is in good agreement with Chang's studies with respect to direct propylene epoxidation using OOH* on Au_{38} particles (Chang et al., 2011). In addition, both of these studies and some other groups have demonstrated another possible pathway for PO production via an oxametallacycle intermediate (OMMP, oxygen-metal-metal-propylene, a five-member ring) on Au_7/α-Al_2O_3, Au(3 2 1), Ag(1 1 1), respectively (Liu et al., 2016; Moskaleva, 2016; Torres et al., 2007). However, instead of an extended metal surface, the experimental samples in our current work have been prepared with atomic-layer deposition (Lu et al., 2018), resulting in isolated Ti sites, which indicates that the OMMP intermediate with two neighboring Ti atoms incorporated is unlikely. Therefore, an OMP intermediate is used in our KMC model, namely, OMC′ or OMC″ as described in Scheme 2, depending on the specific oxygen-carbon binding to propylene.

Furthermore, several byproducts coproduced in the propylene epoxidation reaction are taken into consideration in this work, since they are capable of affecting the PO selectivity and catalyst activity. For instance, the isomerization of PO and its oxidative cracking at high temperature were regarded as the main reaction channels giving rise to the low PO selectivity observed experimentally (Chen et al., 2011; Stangland et al., 2000). Some groups also proposed that PO oligomerization or its further oxidation into acids resulted in catalyst deactivation due to the poisoning of active sites (Nijhuis et al., 1999; Nijhuis et al., 2005b; Uphade et al., 2002).

The reaction network in our KMC simulations is involved in two different reaction zones as shown in Fig. 2 instead of a single reaction domain (e.g., single metal surface) over $Au/TiO_2/SiO_2$. An interfacial reaction network shown in Scheme 2 is implemented into the KMC model to simulate the PO reaction and relevant side reactions (reaction zone Ω2 in Fig. 2). Additionally, it was suggested that the allylic hydrogen stripping of propylene leading to acrolein is always challenging for PO commercial production (Dai et al., 2017; Stangland et al., 2000; Wells et al., 2004a). The acrolein formation proceeds on Au nanoparticles (reaction zone Ω1 in Fig. 2), and its relevant side reaction channels have been proposed in Scheme S1 in Supporting Information.

Overall, a reaction network consisting of 60 events (Table S1) is included in the KMC model which can account for changes in the reaction temperature, the varying H_2/C_3H_6 inlet concentration ratio and O_2 feed concentration. The species desorbing into the bulk gas phase are product PO, the main byproduct acrolein, and other side products propanal, acetone, and ethanal.

4. Results and discussion

4.1. Benchmarking of KMC model

Previous theoretical investigations have demonstrated that the calculated active barrier of the direct epoxidation step between H_2O_2 and C_3H_6 to be 19.9 kcal/mol within TS-1 catalyst pores, whereas the local structure can shift this value to as low as 9.3 kcal/mol near surface defects (Joshi et al., 2007a,b; Wells et al., 2004a). Simultaneously, previous experimental studies regarding the direct PO reaction on Au/TS-1 and Au-Ti-TUD catalysts have been used to empirically estimate an active barrier of 8.4–13.1 kcal/mol (Lu et al., 2007; Taylor et al., 2006).

As shown in Scheme 2, the PO reaction undergoes two elementary steps: the oxametallacycle (OMP: OMC' or OMC'') formation along with the O—OH cleavage of OOH* species, and the ring contraction of OMP toward PO. The former one, OMP formation, is a slow reaction in contrast with its further isomerization. The active barrier for forming OMP is calculated to vary over a range of 6.70–18.40 kcal/mol on an Au(3 2 1) surface depending on the different Au sites, and is 19.13 kcal/mol on Au_{38} (Chang et al., 2011; Moskaleva, 2016), which is very close to the calculated value of 19.9 kcal/mol on the ideal TS-1 aforementioned using H_2O_2 as the active oxidant in the model.

A preliminary test in our simulations shows that using the active barrier (>19.0 kcal/mol) for the OMP formation leads to a predicted PO formation rate lower than the experiments. Furthermore, this high E_a value brings about a statistical sampling challenge, and hence we have artificially lowered the barrier of OMP formation (reactions # 42 and 44 in Table S1) over a range of 11.0–15.0 kcal/mol. The active barriers of the rate-limiting steps

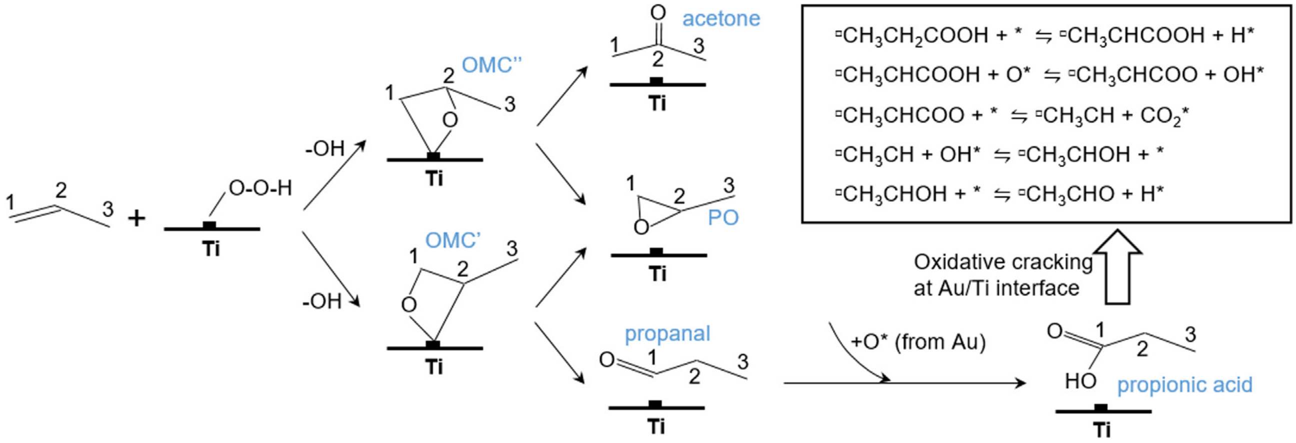

Scheme 2. Proposed reaction network at the Au/Ti interface (reaction zone Ω2 in Fig. 2). The * symbol represents a bare Au site, and □ represents a bare interfacial Ti site that is in contact with Au nanoparticles (for clarity, Au nanoparticle is not shown here). The species attached to * or □, indicates one Au surface-bound species or one Ti surface-bound species, respectively.

(reactions # 27, 34, 51, and 56 in Table S1) of side reactions are accordingly reduced by an equivalent amount. With this range of artificially-low values, the overall PO formation rates predicted from the KMC simulations follow an Arrhenius relationship as demonstrated in Fig. S1 in Supporting Information, so that the behavior at higher E_a values can be easily extrapolated. The correlation coefficients for the four fitted trend lines in Fig. S1 are over 0.999. The slopes of the trend lines in Fig. S1 are −1.102, −1.096, −1.171 and −1.223 at 413, 433, 453 and 473 K, respectively. When the KMC data are extrapolated to the higher E_a values, the results can be closely aligned with the experimental findings. For a fair comparison between simulation activities and experiments, the PO formation rate as a function of the rising reaction temperature is plotted in Fig. 3. It is clearly seen that the formation rates of PO predicted by the KMC simulations fall within reasonable agreement of the experimental results (with an E_a value of 17.45 kcal/mol).

In the following sections, simulation conditions are evaluated with KMC to predict the impact of different reaction conditions on PO and side product formation, along with experimental comparisons. Then, a detailed reaction mechanism is proposed in Section 5, along with strategies for enhancing PO activity.

4.2. Effect of reaction temperature

Using the KMC model evaluated in Section 4.1, the reaction temperature can now be altered to analyze its impact on the selectivity of PO and side products. The feed concentration of H_2, O_2, and C_3H_6 is set at 10%, similar to experiments. In the experimental data used to evaluate our model, CO_2 is not detected in the final gas product mixture, and this is probably due to the insensitivity of the thermal conductivity detector (TCD) used. However, the simulations predict measurable amounts of CO_2, which is also found in previous experiments (Lee et al., 2012; Stangland et al., 2000; Uphade et al., 2002). In order to compare with experimental findings, CO_2 produced in the KMC simulations is not accounted for in the selectivity calculations. The detailed results concerning the selectivity of products including CO_2 have been compiled in the corresponding sections of the Supporting Information. It can be observed that under various reaction conditions, the selectivity of CO_2 is very low, only about 1%, which is lower than experimentally reported 2–4% using Au/T-S(α) catalyst and 4–8% in the catalyst Au/Ti-MCM-48 (Stangland et al., 2000; Uphade et al., 2002).

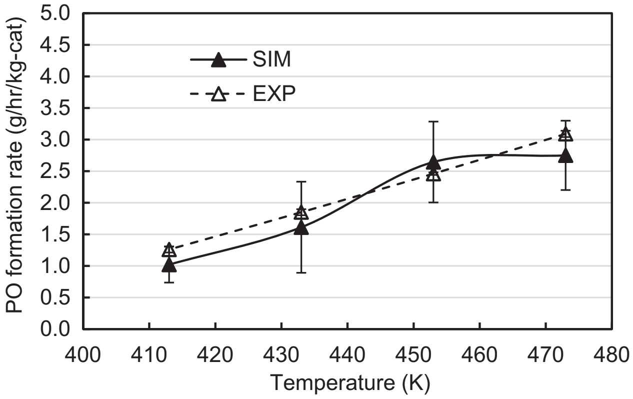

Fig. 3. Comparison of experimental (Lu et al., 2018) and predicted KMC simulation of the PO formation rates, achieved using an extrapolated E_a value of 17.45 kcal/mol for the OMP formation step. The error bars indicate the standard deviation, which is smaller than the symbol in some cases. The feed concentration of H_2, O_2, and C_3H_6 is set at 10%, similar to experiments.

In spite of a growing PO formation rate with the increasing reaction temperature as exhibited in Fig. 3, Fig. 4a demonstrates that the PO selectivity experimentally has decreased by ~10% as the temperature rises from 413 to 473 K, suggesting a strong negative temperature dependence of PO selectivity. The KMC simulations nicely reproduce this declining trend toward PO selectivity. Furthermore, it is clearly seen that the selectivity to byproducts, such as acrolein and propanal, acetone, and ethanal (Fig. 4b–d), is growing from both experiments and simulation results, which reflects an apparently positive correlation with the rising temperature. In particular, the selectivity of acrolein and propanal has increased from 4% to 11% as shown in Fig. 4b. For a fair comparison with the combined selectivity of acrolein and propanal experimentally, the sum of the selectivity toward acrolein and propanal is computed during the KMC simulations. However, the KMC simulations predict that the selectivity to acrolein is much higher than propanal due to the facile acrolein formation (as discussed below).

It has been suggested in the literature that acetone and propanal are derived from PO isomerization at the gold-titania interface, and the oxidative cracking of PO contributes to increasing ethanal and CO_2 formation at higher temperature (Chen et al., 2011; Stangland et al., 2000). Inspired by the ethylene oxide (EO) formation via an oxametallyacycle (OME or OMME) on the Ag surface (Jones et al., 1998; Linic and Barteau, 2002; Linic et al., 2002), we propose an alternative interpretation for the trends in Fig. 4, involving OMP. As stated before, OOH* generated on the Au surface either decomposes or transfers to the neighboring Ti site to form the true active oxidant Ti–OOH species. When propylene approaches Ti–OOH, its C=C double bond encounters the electrophilic reaction with Ti–OOH, to form an OMP complex (OMC′ or OMC″ in Scheme 2) by the abstraction of the hydroxyl at the interfacial Ti site. The formed OMP can either undergo a ring closure to yield a new three-member ring, PO, or undergo a 1,2-H shift reaction to form acetone or propanal. The isomerization of OMP toward PO is much easier than forming acetone or propanal since the latter has a much higher active barrier (13.05 vs. 15.00 kcal/mol in Table S1). Nonetheless, as the reaction temperature grows, the evolution of OMP toward acetone or propanal proceeds much more readily and hence weakens the PO formation, since the slow reaction (with a higher active barrier) is much more sensitive to higher temperature. Infrared spectra has previously suggested that ketone or aldehyde species form out of a so-called bidentate propoxy species intermediate after PO adsorption on Au/TiO_2 (Nijhuis et al., 2005a,b). We infer that this bidentate propoxy species is one possible intermediate which is functionally similar but structurally different from OMP, since most Ti sites are isolated in our model and experiments. Therefore, we propose that the oxametallacycle OMP is the precursor for parallel reaction channels toward PO, acetone, and propanal at the interfacial Ti sites, similar to the EO production on an Ag surface (Özbek and van Santen, 2013).

Upon the increasing selectivity of ethanal with the rising reaction temperature (Fig. 4d), propanal is formed through a ring-opening of OMP at the interfacial Ti site. It is first oxidized into propionic acid (or propionate) by O* from the adjacent Au nanoparticles, and then it undergoes a decarboxylation process with the aid of O* and H* from the Au surface. After the CO_2 abstraction from carboxylates, the leading fragment CH_3CH (sitting on the dual interface Ti site) is subsequently bonded with one neighboring hydroxyl (sitting on the dual interface Au site), and further forms ethanal via H-stripping. The decarboxylation of carboxylic acids or carboxylates have been reported on Pt, Pd and Au surfaces both theoretically and experimentally (Basaran et al., 2013; Lu et al., 2012; Nijhuis et al., 2005a; Siler et al., 2014). The R–COO scission is the rate-limiting step (with a high E_a) in decarboxylation, and it is particularly sensitive to elevated reaction temperatures.

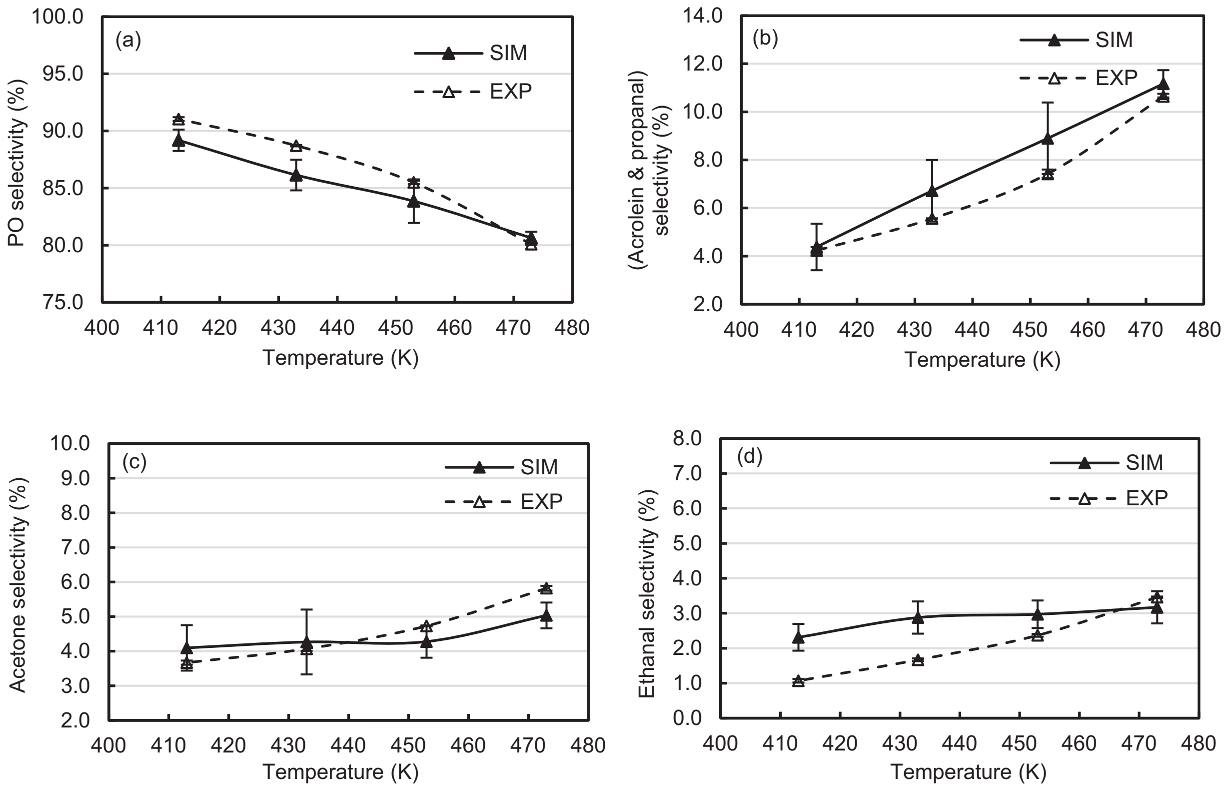

Fig. 4. Selectivity comparison of (a) PO, (b) acrolein and propanal, (c) acetone, and (d) ethanal from both extrapolated simulations and experiments (Lu et al., 2018) as a function of the reaction temperature. The feed concentration of H_2, O_2, and C_3H_6 is set at 10%.

Consequently, the R–COO cleavage becomes much easier as the reaction temperature increases, giving rise to more ethanal and CO_2. It should be pointed out that ethanal may be further oxidized into acetic acid and then experience a C—C bond breakage to form methane, formaldehyde, ethane, and more CO_2 (Cremer et al., 2014; Siler et al., 2014). But such species are not detected or negligible in the current experiments, probably due to the limited temperature range (<475 K) or limited O^* concentration on the Au surface. Thus, we did not include the oxidative cracking pathways of ethanal in our KMC model.

Acrolein is generally considered to be the most significant byproduct from the propylene epoxidation reaction (Stangland et al., 2000). According to Fig. 4b, the selectivity of acrolein and propanal substantially increases with the elevated temperature. In comparison to propanal, acrolein formation contributes more to this trend, since propanal is formed at a rate almost equivalent to acetone (same isomerization barrier from OMP in Table S1), while the increasing selectivity to acetone (Fig. 4c) is not as remarkable. Meanwhile, propanal is also subjected to oxidative cracking into ethanal and CO_2. Unlike PO and other byproducts occurring at the interfacial Au/Ti sites, acrolein can be formed on Au nanoparticles without Ti sites involved (Stangland et al., 2000). After propylene adsorption on Au particles, it undergoes allylic hydrogen abstraction by surface O^*, since its methyl hydrogen is facile and acidic. The nucleophilic attack of O^* on allylic hydrogen of propylene leads to allyl formation, which then binds with another O^* to form allyloxy, as suggested in previous studies (Dai et al., 2017; Moskaleva, 2016; Wells et al., 2004a). Acrolein is easily derived from the allyloxy through H-abstraction (see Scheme S1 in Supporting Information). The ease of allylic hydrogen stripping brings about the remarkably increased selectivity of acrolein with the rising reaction temperature, as seen in Fig. 4b.

Friend et al. proposed that the allyloxy formation occurred via the direct insertion of O^* into one of the allylic C—H bonds, followed by the allylic hydrogen transfer to a surface O^* adsorbed on Au(1 1 1) without allyl formation, which is slightly different from the reaction pathway in our KMC simulations (Deng et al., 2006; Liu and Friend, 2010). Both routes involving allyl (or not) seem feasible for the allyloxy formation, but we suggest that the direct allyloxy formation in Friend's studies is associated with exceptionally high O^* coverage. In our propylene epoxidation system, the atomic O^* concentration on Au particles are rather low (0.0289–0.0576, $413\text{ K} \le T \le 473\text{ K}$), and far from the O-covered Au(1 1 1) condition used by the Friend group.

It is worthwhile to note that propanal formation originates not only from the isomerization of OMC' at the interfacial Ti site aforementioned, but also from the hydrogenation of acrolein on Au nanoparticles, although the former is clearly dominant according to our simulation results. As a consequence, the oxidation of propanal into propionic acid by surface O^* as well as subsequent decarboxylation leading to CO_2 and ethanal, can also occur on Au nanoparticles (see Scheme S1 in Supporting Information).

In addition, an analysis of O^* coverage on Au nanoparticles has been performed to gain insight into the varying selectivity of products with the increasing reaction temperature. Atomic O^* is primarily formed out of H_2-O_2 related reactions on Au nanoparticles involving reactions # 4, 5, 11, 14, and 15 in Table S1, while O^* is mainly consumed by side reactions involving reactions # 25, 26, 31, 33, 53, and 55. As the reaction temperature rises from 413 to 473 K, Fig. 5 shows that the O^* coverage on the Au surface has drastically declined by ~50%, indicating that the consumption rate of O^* by side reactions (e.g., the formation of acids and its oxidative cracking, allylic hydrogen stripping by O^*) becomes much faster than its formation rate (see Section S3 in Supporting Information). Therefore, the decreasing trend of surface O^* coverage with the

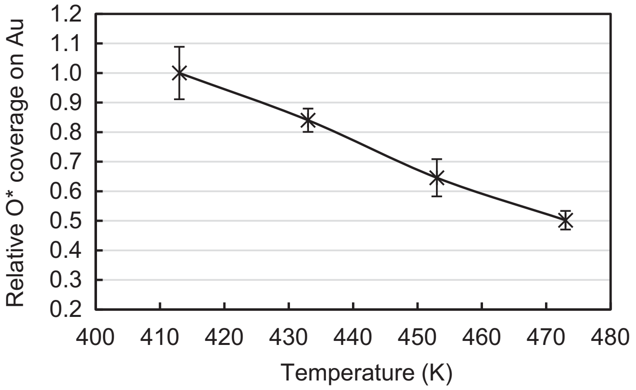

Fig. 5. Relative change in the atomic O* coverage (the reference value is 0.0576 at 413 K) on Au nanoparticles as a function of the reaction temperature. The feed concentration of H_2, O_2, and C_3H_6 is set at 10%.

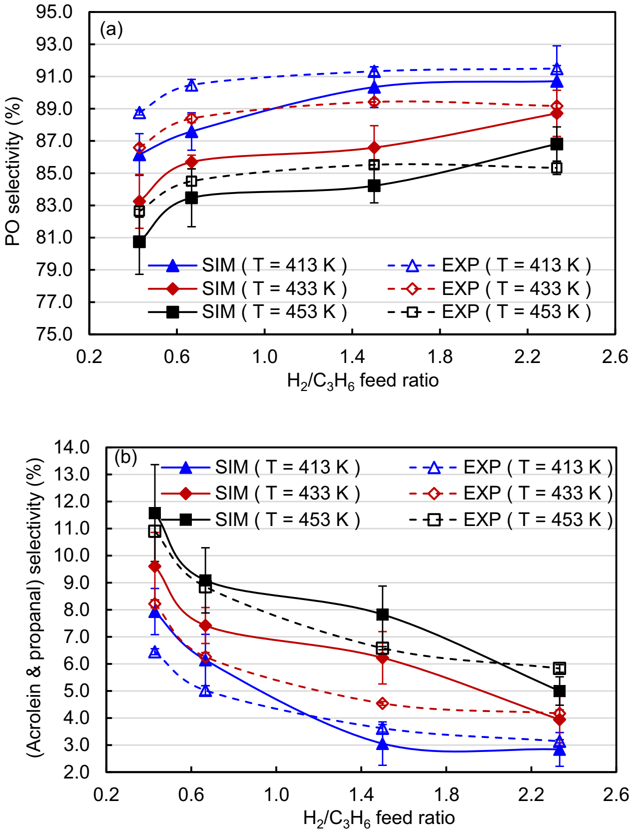

Fig. 6. Selectivity comparison of (a) PO and (b) acrolein and propanal from both extrapolated simulations and experiments (Lu et al., 2018) as a function of H_2/C_3H_6 feed concentration ratio, at different reaction temperatures. The feed concentration of O_2 is set at 10%.

increasing reaction temperature provides an additional indicator for the growing selectivity of byproducts (Fig. 4b–d), corresponding to the decreasing PO selectivity (Fig. 4a).

By a coverage analysis of surface species, we also note that almost no carboxylic acids or carboxylates sit on the Au/Ti dual interface sites or Au surface sites within the temperature range (413–473 K). These carboxylic acids or carboxylates, derived from the oxidation of ketone and aldehyde species as discussed before, were regarded as the key species responsible for the catalyst deactivation under relatively low reaction temperatures (e.g., <373 K) because of site-blocking (Nijhuis et al., 2005a,b; Stangland et al., 2000). However, at much higher temperatures (e.g., >400 K in this work), the decarboxylation (oxidative cracking) of carboxylates proceeds rapidly, so that interfacial Au/Ti sites continue to act as active sites for PO production, and thus catalyst deactivation is not expected to be relevant to the conditions of our study. Meanwhile, neither the KMC simulations nor the experiments capture dioxanes or 2,5-dimethyl-1,4-dioxane in the final gas products or on the catalyst surface, although previous experiments suggested such species formed from PO oligomerization could reduce epoxidation yield (Nijhuis et al., 1999; Uphade et al., 2002). An analysis of Ti sites on the SiO_2 surface from the KMC model (~10%) and the experimental catalysts (~9.7%) indicates that Ti sites are highly dispersed and few Ti sites are adjacent, thus suppressing PO oligomerization.

4.3. Effect of H_2/C_3H_6 feed ratio

The H_2/C_3H_6 feed concentration ratio is varied in order to analyze its influence on the selectivity of PO and side products, while keeping the O_2 inlet concentration constant (10%), similar to the experiments. The inlet concentration of H_2 is increased from 6%, 8%, 12%, to 14%, as the corresponding C_3H_6 inlet concentration is decreased from 14%, 12%, 8%, to 6%, respectively. Thus, the H_2/C_3H_6 feed concentration ratio is increasing from 6/14 (0.43) to 14/6 (2.33).

Fig. 6a displays the increasing selectivity to PO as the H_2/C_3H_6 inlet ratio increases from 0.43 to 2.33 at each experimental reaction temperature (413, 433, and 453 K), and the KMC simulations qualitatively capture this trend. While the simulation results demonstrate a slightly greater sensitivity of PO selectivity to the H_2/C_3H_6 inlet ratio than the corresponding experiment, the large error bars on the KMC data are somewhat larger. Simultaneously, it can be unambiguously shown that PO selectivity is declining with the temperature rising from 413 to 453 K based on both simulations and experiments (Fig. 6a), which is consistent with the discussions in Section 4.2. Nonetheless, along with the increasing H_2/C_3H_6 feed concentration ratio, both KMC simulations and experimental data demonstrate that the selectivity to acrolein and propanal significantly drops, by 3–6%, depending on the reaction temperature (Fig. 6b). We also note that the selectivity toward acrolein and propanal increases as the reaction temperature rises from 413 to 453 K, which is again in line with the previous discussions.

The increasing selectivity of PO (Fig. 6a) along with the growing H_2/C_3H_6 inlet ratio at each reaction temperature is most likely ascribed to the fact that excessive hydrogen accelerates the formation of OOH* ($H^* + O_2^* \leftrightharpoons OOH^* + *$, reaction # 8 in Table S1), which then spills over to the adjacent Ti site to form active Ti–OOH species that epoxidizes C_3H_6 into more PO. Meanwhile, the increasing surface H* arising from the growing H_2/C_3H_6 inlet ratio, will consume more surface O* to help reduce O* coverage according to $O^* + H^* \leftrightharpoons OH^* + *$ (reaction # 5). However, an analysis of O* coverage demonstrates that the O* concentration on the Au surface slightly increases with the increasing H_2/C_3H_6 inlet ratio, as seen in Fig. 7. This is because there are several other reactions involved that also contribute to O* generation (at a faster rate with the growing H_2/C_3H_6 inlet ratio): $OH^* + OH^* \leftrightharpoons H_2O^* + O^*$ (reaction # 11), $H_2O_2^* + * \leftrightharpoons H_2O^* + O^*$ (reaction # 14), and $OOH^* + * \leftrightharpoons OH^* + O^*$ (reaction # 15) in Table S1.

As mentioned before, atomic O* participates in a series of side reactions leading to byproducts (e.g., acrolein, acid, ethanal, etc.). One may ask, since more atomic O* is produced, why the selectivity to acrolein and propanal noticeably decreases with the increasing H_2/C_3H_6 inlet ratio (especially considering the fact that acrolein formation derived from the allylic hydrogen stripping by surface

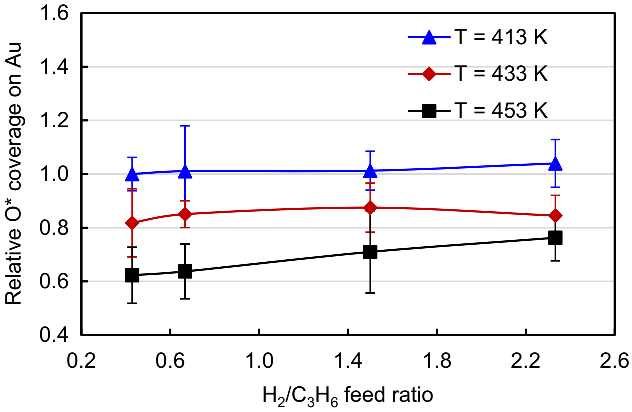

Fig. 7. Relative change in atomic O^* coverage (the reference value is 0.0532 at 413 K and H_2/C_3H_6 = 0.43) on Au nanoparticles as a function of H_2/C_3H_6 feed concentration ratio under different reaction temperatures. The feed concentration of O_2 is set at 10%.

O^* on Au nanoparticles is facile). It is most likely that the atomic O^* concentration on the Au surface is sufficient (and not a limiting factor) for acrolein formation.

We infer that the competitive adsorption of C_3H_6 on two various reaction zones described in Fig. 2, namely, the Au/Ti dual interface sites (yielding PO) and Au nanoparticles (yielding acrolein), accounts for the effect of the increasing H_2/C_3H_6 feed concentration ratio on inhibiting acrolein production. From previous studies, C_3H_6 is prone to adsorb on the interfacial Ti sites, versus the Au nanoparticle surfaces (Ajo et al., 2002; Bravo-Suárez et al., 2007; Taylor et al., 2006). Increasing the hydrogen gas concentration increases the surface H_2^* and H^* species (H_2^* dissociation into $2H^*$) on the Au nanoparticles. Then, H^* species bind surface O_2^* to form more OOH^* and further Ti–OOH^*, which will consume more C_3H_6. In turn, this allows more C_3H_6 adsorption and reaction at interfacial Ti sites to accelerate PO production.

Meanwhile, as the H_2/C_3H_6 feed concentration ratio increases, the competitive adsorption between H_2 and C_3H_6 on Au nanoparticles (reaction zone Ω1 in Fig. 2) also serves to suppress the formation of acrolein, since both the coverages of H_2^* and H^* on the Au surface increase (Fig. S3 in Supporting Information). Due to the competition of H_2 adsorption on Au nanoparticles, the adsorption of C_3H_6 on the Au particle surface is impaired with the increasing H_2/C_3H_6 inlet ratio, leading to less acrolein formation. A slightly increasing O^* coverage (Fig. 7) on the Au surface with the rising H_2/C_3H_6 inlet ratio indicates that side reactions consuming O^* are weakened, in particular, the formation of acrolein, the most significant byproduct.

However, it should be pointed out that the increasing hydrogen feed concentration from 6% to 14% mentioned above is accompanied by the decreasing C_3H_6 feed concentration from 14% to 6%. One might wonder whether the decreasing C_3H_6 feed concentration is also responsible for the reduced acrolein selectivity. Thus, additional simulations have been performed with the hydrogen inlet concentration increasing from 6% to 14% while keeping both C_3H_6 and O_2 feed concentrations constant (at 10%). As the hydrogen inlet concentration grows, the increased PO selectivity and the reduced acrolein and propanal selectivity are indeed captured (Fig. S4 in Supporting Information). Meanwhile, the increased O^* coverage on the Au surface is also observed with the increasing H_2 feed concentration (Fig. S5 in Supporting Information), suggesting that the allylic hydrogen abstraction of C_3H_6 by surface O^* (leading to acrolein) is impaired. Such results indicate that the dropping selectivity toward acrolein is not caused by the decreasing C_3H_6 feed concentration.

Furthermore, an analysis of the consumption rate of C_3H_6 at the two different reaction zones demonstrates that as the H_2 concentration increases: 1) the consumption rate of C_3H_6 at interfacial Ti sites to yield PO is increasing, and 2) the consumption rate of C_3H_6 on Au particles to form acrolein is also growing (while PO formation increases faster, see Figs. S6 and S7 in Supporting Information). We argue that the adsorption of C_3H_6 on the Au nanoparticles competes with H_2 adsorption on the Au nanoparticles (as well as with C_3H_6 adsorption at the interfacial Ti sites), leading to less acrolein formation and a decreasing selectivity. Therefore, all these results stress the significance of an optimal H_2/C_3H_6 inlet ratio for balancing the selectivity of PO and the byproduct acrolein.

Previous adsorption studies have demonstrated that C_3H_6 readily adsorbed on the low-coordinated sites (e.g., edge, corner sites) of Au particles (Ajo et al., 2002; Driscoll et al., 2017; Panayotov et al., 2016), while in the present simulations all Au sites are treated equally. Thus, implementing differential adsorption energies for C_3H_6 on the Au surface (corners, edges, steps) is an opportunity for the future model improvement.

As stated previously, in parallel to OOH^* spillover to the neighboring Ti sites to form Ti–OOH species, it is likely that more OOH^* is involved in decomposition or degradation into OH^* (H_2O^*) and O^* as the hydrogen feed concentration increases. Thus, we have analyzed the frequency of elementary reactions # 42 and 44 in Table S1 toward OMP formation via Ti–OOH intermediates as well as the elementary step # 15 concerning the OOH^* decomposition ($OOH^* + * \leftrightharpoons OH^* + H^*$). This allowed us to calculate the ratio of OMP formation versus OOH^* decomposition as a function of the hydrogen feed concentration. As seen from Fig. 8, this ratio decreases, indicating that the hydrogen utilization efficiency decreases as the hydrogen feed concentration increases, which is in accordance with previous experimental reports (Huang and Haruta, 2012; Stangland et al., 2000). The ease of OOH^* ($H_2O_2^*$) degradation or decomposition is a significant challenge in enhancing hydrogen efficiency (Chen et al., 2011), emphasizing that a proper H_2/C_3H_6 feed concentration ratio is crucial for the efficient utilization of active OOH^* species. In order to address this issue, supports with hydrophobic surfaces may help suppress the decomposition of hydroperoxide species (Huang and Haruta, 2012). Screening for the optimum Au particle size and support may reduce the decomposition of OOH^* and $H_2O_2^*$ species. In addition, the particle-support interaction may affect the wetting and morphology of the Au nanoparticles, leading to a varying number of Au/Ti dual interfacial sites, as well as active Au sites which influence the formation site of OOH^* (and its diffusion distance toward adjacent Ti sites).

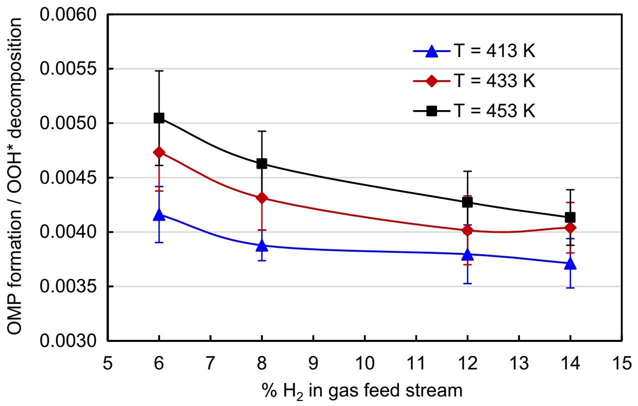

Fig. 8. Ratio of OMP formation rate to OOH^* decomposition rate as a function of H_2 feed concentration, at different reaction temperatures. Both C_3H_6 and O_2 feed concentrations are set at 10%.

Table 1
Selectivity comparison of acetone from both simulations and experiments (Lu et al., 2018) at different gas feed compositions and reaction temperatures. Standard deviations are indicated in parentheses. The feed concentration of O_2 is set at 10%.

	Composition		T = 413 K		T = 433 K		T = 453 K	
H_2/C_3H_6	% H_2	% C_3H_6	SIM	EXP	SIM	EXP	SIM	EXP
0.43	6	14	3.70 (0.40)	3.87 (0.06)	4.45 (1.09)	3.99 (0.11)	4.48 (0.52)	4.48 (0.08)
0.67	8	12	3.86 (0.59)	3.62 (0.15)	4.39 (0.53)	3.87 (0.08)	4.57 (0.79)	4.52 (0.02)
1.50	12	8	3.98 (0.39)	3.86 (0.13)	4.41 (1.07)	4.12 (0.16)	4.62 (0.56)	5.18 (0.03)
2.33	14	6	3.92 (0.95)	3.74 (0.30)	4.61 (0.49)	4.52 (0.05)	4.95 (0.73)	5.64 (0.11)

Table 2
Selectivity comparison of ethanal from both simulations and experiments (Lu et al., 2018) at different gas feed compositions and reaction temperatures. Standard deviations are indicated in parentheses. The feed concentration of O_2 is set at 10%.

	Composition		T = 413 K		T = 433 K		T = 453 K	
H_2/C_3H_6	% H_2	% C_3H_6	SIM	EXP	SIM	EXP	SIM	EXP
0.43	6	14	2.21 (0.68)	0.92 (0.03)	2.69 (0.28)	1.19 (0.05)	3.21 (0.14)	1.97 (0.09)
0.67	8	12	2.41 (0.21)	0.89 (0.05)	2.50 (0.47)	1.48 (0.13)	2.88 (0.09)	2.13 (0.04)
1.50	12	8	2.63 (0.23)	1.19 (0.11)	2.78 (0.27)	1.92 (0.09)	3.33 (0.43)	2.72 (0.15)
2.33	14	6	2.53 (0.92)	1.63 (0.34)	2.74 (0.48)	2.14 (0.04)	3.24 (0.82)	3.20 (0.17)

Table 3
Selectivity comparison of PO and main byproducts, acrolein and propanal, acetone, and ethanal from both simulations and experiments (Lu et al., 2018) at different O_2 feed concentration with temperature fixed at 453 K. Standard deviations are indicated in parentheses. Both C_3H_6 and H_2 feed concentrations are set at 10%.

	PO		Acrolein & propanal		Acetone		Ethanal	
% O_2	SIM	EXP	SIM	EXP	SIM	EXP	SIM	EXP
4	83.33(1.78)	85.15(0.33)	9.65(1.09)	6.47(0.14)	4.34(0.97)	6.01(0.12)	2.68(0.70)	2.38(0.12)
6	83.72(1.11)	85.51(0.05)	8.97(1.25)	6.78(0.04)	4.44(0.71)	5.30(0.08)	2.87(0.49)	2.41(0.06)
8	82.44(0.98)	85.58(0.13)	9.56(0.88)	7.19(0.10)	4.50(0.54)	4.95(0.08)	3.50(0.27)	2.28(0.10)
10	83.84(1.74)	85.49(0.15)	8.33(1.37)	7.42(0.18)	4.27(0.43)	4.73(0.01)	3.06(0.41)	2.37(0.04)

There are two different reaction routes for propanal formation in our KMC model as mentioned in Section 4.2, either from OMC’ isomerization at the interfacial Ti sites or from acrolein hydrogenation on Au nanoparticles. The increasing H_2/C_3H_6 concentration ratio leads to more OOH* and Ti–OOH formation, and further OMC’ formation at the interfacial Ti sites. In comparison with the PO formation through the ring closure of OMC’, the ring-opening route toward propanal formation with H-transfer has to overcome a much higher barrier (13.05 vs. 15.00 kcal/mol in Table S1). As a consequence, propanal production from OMC’ evolution slightly increases. Thus, it is not as sensitive to the increasing hydrogen concentration as it is to the rising reaction temperature. Additionally, the propanal originating from acrolein hydrogenation drops, since acrolein production is weakened by the increasing hydrogen concentration. Therefore, a decreasing selectivity to acrolein and propanal is observed from both the experiments and KMC simulations as the H_2/C_3H_6 inlet ratio increases, as demonstrated in Fig. 6b.

As reported in Tables 1 and 2, the selectivity to acetone and ethanal is generally increasing as the H_2/C_3H_6 inlet ratio grows at each reaction temperature. The KMC simulations do not predict a monotonic increase in selectivity to acetone and ethanal as the H_2/C_3H_6 inlet ratio grows, while the relatively larger standard error associated with the KMC simulation data may account for this fluctuation.

Although the selectivity of PO and acrolein and propanal (Fig. 6) show large variations, it is clearly seen that the selectivity toward acetone and ethanal slightly increases with the elevated H_2/C_3H_6 feed concentration ratio. Like the propanal formation arising from OMC’, the acetone production due to OMC“ isomerization has a much larger activation energy than the contraction of the OMC” ring toward PO (13.05 vs. 15.00 kcal/mol in Table S1) (Moskaleva, 2016; Stangland et al., 2000). Thus, only a small fraction of OMC“ evolves toward acetone compared with PO, since the activation energy of OMC” isomerization toward acetone is less sensitive to the increasing hydrogen concentration versus the temperature (Fig. 4c). Similarly, ethanal formation originating from C—C cleavage (rate-limiting step) of carboxylates (Basaran et al., 2013; Lu et al., 2012), is also more sensitive to the temperature than to a higher hydrogen inlet concentration. However, the latter brings about increasing surface concentrations of O* and H*, which assists the formation of acids and the subsequent decarboxylation (Stangland et al., 2000).

4.4. Role of varying O_2 feed pressure

The impact of varying O_2 concentration on the selectivity of products is investigated with the feed concentration of H_2 and C_3H_6 fixed at 10%. The reaction temperature is 453 K, similar to the experiments. From the Table 3, it is found that the selectivity to PO and byproducts based on experimental data varies little as the O_2 inlet concentration increases from 4% to 10%. The KMC simulations demonstrate similar trends (Table 3).

It is well known that O_2 adsorbs on Au particles very weakly and the direct O_2^* dissociation into O* hardly proceeds because of the high activation energy (above 25 kcal/mol) (Chang et al., 2011; Xu and Mavrikakis, 2003). It is likely that the slight effect of O_2 concentration on the selectivity of products (Table 3) should be attributed to the fact that O_2 does not directly participate in kinetically relevant steps for yielding PO (e.g., OMP formation and further isomerization) and byproducts (e.g., the O* involvement). The increasing O_2 inlet concentration corresponds to a slightly increasing coverage of surface O_2^* due to the weak adsorption, leading to a slight increase in OOH* species ($O_2^* + H^* \rightleftharpoons OOH^*$

+ *). In comparison with OOH* used for OMP formation, more OOH* species can also degrade to water and O*, resulting in an increased O* coverage on Au nanoparticles (Fig. S8 in Supporting Information). As a consequence, the formation of PO, propanal, and acetone originating from OMP isomerization changes little, as well as ethanal which is derived from the decarboxylation of propionic acids (or propionates). This is consistent with Chen's studies, in which they suggested that O_2^* serves to stabilize the surface H* and inhibit the redundant formation of peroxo species (Chen et al., 2011).

Due to weak O_2 adsorption on Au particles, the slightly increased O_2 adsorption caused by an elevated O_2 feed concentration is not able to significantly compete with the C_3H_6 adsorption on the Au surface. Therefore, acrolein formation, arising from the methyl hydrogen elimination of C_3H_6 by surface O*, is almost unchanged with respect to the elevated O_2 feed concentration. The slight effect of oxygen presented here is consistent with the kinetic tests of Taylor and Chen (Chen et al., 2011; Taylor et al., 2006), in which they observe a much stronger dependence of PO production on hydrogen feed concentration (versus oxygen).

5. Proposed reaction mechanism

Several reaction mechanisms have been employed to describe the direct propylene epoxidation reaction, since it was first put forward by Haruta (Hayashi et al., 1998). These proposed mechanisms assume that either $H_2O_2^*$ or OOH* is used to epoxidize propylene into PO either on a single-crystal Au surface, Au nanoparticles (Chang et al., 2011; Joshi et al., 2006; Moskaleva, 2016), or on Au nanoparticles supported on Al_2O_3 and graphene (Liu et al., 2016; Pulido et al., 2012). In these mechanisms, a reasonable proximity between Au nanoparticles and Ti sites is emphasized but without specifying an exact reaction zone (Fujitani et al., 2009; Ojeda and Iglesia, 2009; Wells et al., 2004a). Several kinetic studies indicate a mechanism requiring a Au/Ti interface for PO formation but without taking into account any byproduct reaction pathways (Bravo-Suárez et al., 2007; Perez Ferrandez et al., 2015; Taylor et al., 2006).

In this work, our KMC simulations have successfully reproduced significant aspects of the experimental behavior. A modified

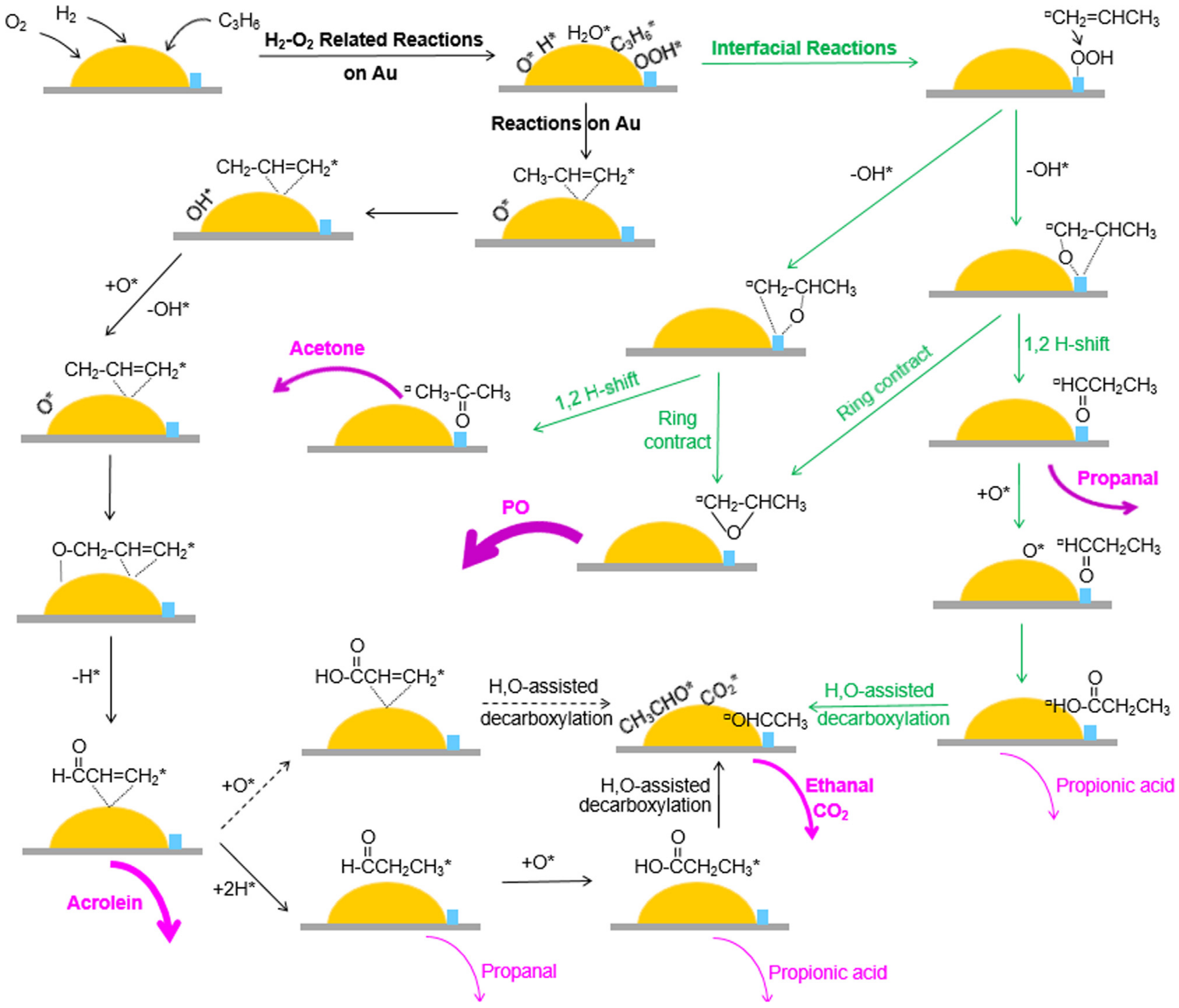

Fig. 9. Proposed reaction mechanism for direct propylene epoxidation over $Au/TiO_2/SiO_2$ (gold/blue/gray). Green coloring indicates interfacial reaction routes, and black coloring is related to reactions on the Au surface. Dashed lines (black) indicate possible reactions occurring during propylene epoxidation, but are not included in the present KMC model. Pink coloring corresponds to products with different weights, indicating relative formation rates. The species attached to * or □, indicates one Au surface-bound species or one Ti surface-bound species, respectively. (For interpretation of the references to colour in this figure legend, the reader is referred to the web version of this article.)

mechanistic model has been proposed, including the PO reaction and key side reaction channels. This mechanism is graphically represented in Fig. 9, and it highlights the Au/Ti dual interface reactions at the periphery of Au nanoparticles and important reactions occurring on the Au surface, according to the following description.

(i) As the $H_2/O_2/C_3H_6$ gas mixture is fed, H_2 and O_2 adsorb on Au nanoparticles and undergo a series of H_2-O_2 related reactions. The dissociated H^* either encounters the combustion steps to produce water or binds with O_2^* to form OOH^* and $H_2O_2^*$ intermediates. In parallel to the degradation or decomposition of hydroperoxy species (OOH^* and $H_2O_2^*$) to water and atomic O^*, OOH^* species may travel to interfacial Ti sites in proximity to form the oxidant Ti–OOH, depending upon its diffusion distance from the interfacial Ti sites. Propylene preferentially approaches the Ti–OOH species and further forms an oxametallacycle OMP, along with hydroxyl stripping. The resulting OMP complex either isomerizes into PO with its ring closure or evolves toward propanal or acetone via a 1,2-H shift. Propanal formed at the interfacial Ti sites is further oxidized into propionic acid (or propionate) by atomic O^* from neighboring Au nanoparticles. Subsequently, the decarboxylation of carboxylates proceeds to produce CO_2 and further ethanal, via a H-assisted step. Ethanal may undergo a similar oxidative cracking process into CO_2 depending on experimental conditions.

(ii) In addition to H_2-O_2 related reactions as stated in (i), the C_3H_6 molecule adsorbed on Au particles encounters the nucleophilic attack of surface O^* on its methyl hydrogen. The ease of allylic hydrogen abstraction facilitates the formation of allyl, and further to allyloxy by binding another surface O^*, giving rise to acrolein by hydrogen elimination. The formed acrolein on the Au nanoparticles can either be hydrogenated into propanal, which then suffers from a series of secondary reactions like the interfacial reactions above, or it can be oxidized into acrylic acid that will likely experience oxidative cracking.

6. Conclusions

In summary, we have demonstrated the capability of KMC simulations for capturing the complex PO reaction network encountered in supported Au catalysts, including the role of side products. This has allowed us to explore open controversies about the propylene epoxidation reaction over gold/titania catalysts and provide atomistic-level rationalization of the observed behavior. The decreasing surface O^* coverage on the Au surface along with the elevated reaction temperature explains the negative effect of high temperature on PO selectivity due to increased byproduct formation, particularly acrolein. The selectivity to PO is more dependent on the hydrogen feed concentration. The increasing hydrogen feed concentration is compromised by a decreasing utilization efficiency of hydrogen due to the decomposition of hydroperoxide species and the combustion of surface H^*. The importance of the H_2/C_3H_6 feed concentration ratio is emphasized, since not only H_2 and C_3H_6 competitively adsorb on the Au nanoparticles, but the adsorption of C_3H_6 itself on the interfacial Ti sites and Au nanoparticles is also competitive, noticeably influencing PO and acrolein formation. The deduced mechanism provides fundamental insight into the synergistic effect of the Au/Ti dual interface sites, thereby highlighting the role of the interfacial region.

To enhance PO production and suppress side product formation, one key point is to lower the atomic O^* concentration, which is primarily caused by the decomposition of the hydroperoxy species on the Au surface. Using small Au clusters may help increase the number of Au/Ti dual interface sites, and further increase the probability of OOH^* spillover to the adjacent Ti sites before decomposing to O^*. In addition, previous experimental investigations of H_2O_2 production using Pd-based catalysts demonstrate that acidic supports or supports with acid treatments enhance H_2O_2 selectivity (Blanco-Brieva et al., 2004; Blanco-Brieva et al., 2010; Kim et al., 2012; Park et al., 2012a; Park et al., 2009a; Park et al., 2012b; Park et al., 2009b). Considering that H_2O_2 is a weak acid, we suggest that the interfacial Ti sites serve as Lewis acids which capture OOH^* species, while Brønsted acidic sites incorporated in supports (e.g., SiO_2, carbon, TS-1, etc.) may provide protons to stabilize OOH^* (Chen et al., 2011; Mul et al., 2001). We further infer that Brønsted acid-functionalized supports may promote OOH^* spillover toward the supports, thereby enhancing the probability of OOH^* transferring to the neighboring Ti sites and reducing OOH^* decomposition to O^* on the Au surface. To the best of our knowledge, this strategy for enhancing PO selectivity has not been methodically investigated.

Acknowledgements

Financial support for this work was provided by the National Science Foundation (CBET-1510485 and CBET-1511820) and a UA System Collaboration Grant.

Appendix A. Supplementary material

Supplementary data associated with this article can be found, in the online version, at https://doi.org/10.1016/j.ces.2018.06.064.

References

Ajo, H.M., Bondzie, V.A., Campbell, C.T., 2002. Propene adsorption on gold particles on TiO_2(110). Catal. Lett. 78, 359–368.

Baker, T.A., Xu, B., Jensen, S.C., Friend, C.M., Kaxiras, E., 2011. Role of defects in propene adsorption and reaction on a partially O-covered Au(111) surface. Catal. Sci. Technol. 1, 1166–1174.

Barton, D.G., Podkolzin, S.G., 2005. Kinetic study of a direct water synthesis over silica-supported gold nanoparticles. J. Phys. Chem. B 109, 2262–2274.

Basaran, D., Genest, A., Lercher, J.A., Rösch, N., 2013. Formation of CO_2 and ethane from propionyl over platinum: a density functional theory study. ACS Catal. 3, 1730–1738.

Blanco-Brieva, G., Cano-Serrano, E., Campos-Martin, J.M., Fierro, J.L.G., 2004. Direct synthesis of hydrogen peroxide solution with palladium-loaded sulfonic acid polystyrene resins. Chem. Commun., 1184–1185

Blanco-Brieva, G., de Frutos Escrig, M.P., Campos-Martin, J.M., Fierro, J.L.G., 2010. Direct synthesis of hydrogen peroxide on palladium catalyst supported on sulfonic acid-functionalized silica. Green Chem. 12, 1163–1166.

Bocquet, M.-L., Loffreda, D., 2005. Ethene epoxidation selectivity inhibited by twisted oxametallacycle: a DFT study on Ag surface-oxide. J. Am. Chem. Soc. 127, 17207–17215.

Bravo-Suárez, J.J., Bando, K.K., Lu, J., Haruta, M., Fujitani, T., Oyama, T., 2008. Transient technique for identification of true reaction intermediates: hydroperoxide species in propylene epoxidation on gold/titanosilicate catalysts by X-ray absorption fine structure spectroscopy. J. Phys. Chem. C 112, 1115–1123.

Bravo-Suárez, J.J., Lu, Dallos, C.G., Fujitani, T., Oyama, S.T., 2007. Kinetic study of propylene epoxidation with H_2 and O_2 over a gold/mesoporous titanosilicate catalyst. J. Phys. Chem. C 111, 17427–17436.

Chang, C.-R., Huang, Z.-Q., Li, J., 2015. Hydrogenation of molecular oxygen to hydroperoxyl: an alternative pathway for O_2 activation on nanogold catalysts. Nano Res. 8, 3737–3748.

Chang, C.-R., Wang, Y.-G., Li, J., 2011. Theoretical investigations of the catalytic role of water in propene epoxidation on gold nanoclusters: a hydroperoxyl-mediated pathway. Nano Res. 4, 131–142.

Chen, J., Halin, S.J.A., Pidko, E.A., Verhoeven, M.W.G.M., Ferrandez, D.M.P., Hensen, E.J.M., Schouten, J.C., Nijhuis, T.A., 2013a. Enhancement of catalyst performance in the direct propene epoxidation: a study into gold–titanium synergy. ChemCatChem 5, 467–478.

Chen, J., Halin, S.J.A., Schouten, J.C., Nijhuis, T.A., 2011. Kinetic study of propylene epoxidation with H_2 and O_2 over Au/Ti-SiO_2 in the explosive regime. Faraday Discuss. 152, 321–336.

Chen, J., Pidko, E.A., Ordomsky, V.V., Verhoeven, T., Hensen, E.J.M., Schouten, J.C., Nijhuis, T.A., 2013b. How metallic is gold in the direct epoxidation of propene: an FTIR study. Catal. Sci. Technol. 3, 3042–3055.

Chowdhury, B., Bravo-Suárez, J.J., Mimura, N., Lu, Bando, K.K., Tsubota, S., Haruta, M., 2006. In situ UV−vis and EPR study on the formation of hydroperoxide species during direct gas phase propylene epoxidation over Au/Ti-SiO_2 Catalyst. J. Phys. Chem. B 110, 22995–22999.

Corma, A., Serna, P., 2006. Chemoselective hydrogenation of nitro compounds with supported gold catalysts. Science 313, 332–334.

Cremer, T., Siler, C.G.F., Rodríguez-Reyes, J.C.F., Friend, C.M., Madix, R.J., 2014. Tuning the stability of surface intermediates using adsorbed oxygen: acetate on Au(111). J. Phys. Chem. Lett. 5, 1126–1130.

Dai, Y., Chen, Z., Guo, Y., Lu, G., Zhao, Y., Wang, H., Hu, P., 2017. Significant enhancement of the selectivity of propylene epoxidation for propylene oxide: a molecular oxygen mechanism. PCCP 19, 25129–25139.

Deng, X., Min, B.K., Liu, X., Friend, C.M., 2006. Partial oxidation of propene on oxygen-covered Au(111). J. Phys. Chem. B 110, 15982–15987.

Driscoll, D.M., Tang, W., Burrows, S.P., Panayotov, D.A., Neurock, M., McEntee, M., Morris, J.R., 2017. Binding sites, geometry, and energetics of propene at nanoparticulate Au/TiO_2. J. Phys. Chem. C 121, 1683–1689.

Düzenli, D., Atmaca, D.O., Gezer, M.G., Onal, I., 2015. A density functional theory study of partial oxidation of propylene on Cu_2O(001) and CuO(001) surfaces. Appl. Surf. Sci. 355, 660–666.

Dybeck, E.C., Plaisance, C.P., Neurock, M., 2017. Generalized temporal acceleration scheme for kinetic Monte Carlo simulations of surface catalytic processes by scaling the rates of fast reactions. J. Chem. Theory Comput. 13, 1525–1538.

Ford, D.C., Nilekar, A.U., Xu, Y., Mavrikakis, M., 2010. Partial and complete reduction of O_2 by hydrogen on transition metal surfaces. Surf. Sci. 604, 1565–1575.

Freakley, S.J., He, Q., Harrhy, J.H., Lu, L., Crole, D.A., Morgan, D.J., Ntainjua, E.N., Edwards, J.K., Carley, A.F., Borisevich, A.Y., Kiely, C.J., Hutchings, G.J., 2016. Palladium-tin catalysts for the direct synthesis of H_2O_2 with high selectivity. Science 351, 965–968.

Fu, Q., Saltsburg, H., Flytzani-Stephanopoulos, M., 2003. Active nonmetallic Au and Pt species on ceria-based aater-gas shift catalysts. Science 301, 935–938.

Fujitani, T., Nakamura, I., Akita, T., Okumura, M., Haruta, M., 2009. Hydrogen dissociation by gold clusters. Angew. Chem. Int. Ed. 48, 9515–9518.

Green, I.X., Tang, W., Neurock, M., Yates, J.T., 2012. Localized partial oxidation of acetic acid at the dual perimeter sites of the Au/TiO_2 catalyst—formation of gold ketenylidene. J. Am. Chem. Soc. 134, 13569–13572.

Haruta, M., 1997. Size- and support-dependency in the catalysis of gold. Catal. Today 36, 153–166.

Haruta, M., Date, M., 2001. Advances in the catalysis of Au nanoparticles. Appl. Catal., A 222, 427–437.

Haseltine, E.L., Rawlings, J.B., 2002. Approximate simulation of coupled fast and slow reactions for stochastic chemical kinetics. J. Chem. Phys. 117, 6959–6969.

Hayashi, T., Tanaka, K., Haruta, M., 1998. Selective vapor-phase epoxidation of propylene over Au/TiO_2 catalysts in the presence of oxygen and hydrogen. J. Catal. 178, 566–575.

Hess, F., Over, H., 2017. Rate-determining step or Rate-determining configuration? The deacon reaction over RuO_2(110) studied by DFT-based KMC simulations. ACS Catal. 7, 128–138.

Hess, F., Sack, C., Langsdorf, D., Over, H., 2017. Probing the activity of different oxygen species in the CO oxidation over RuO_2(110) by combining transient reflection–absorption infrared spectroscopy with kinetic Monte Carlo simulations. ACS Catal. 7, 8420–8428.

Hu, G., Orkoulas, G., Christofides, P.D., 2009a. Regulation of film thickness, surface roughness and porosity in thin film growth using deposition rate. Chem. Eng. Sci. 64, 3903–3913.

Hu, G., Orkoulas, G., Christofides, P.D., 2009b. Stochastic modeling and simultaneous regulation of surface roughness and porosity in thin film deposition. Ind. Eng. Chem. Res. 48, 6690–6700.

Huang, J., Haruta, M., 2012. Gas-phase propene epoxidation over coinage metal catalysts. Res. Chem. Intermed. 38, 1–24.

Huang, J., Takei, T., Akita, T., Ohashi, H., Haruta, M., 2010. Gold clusters supported on alkaline treated TS-1 for highly efficient propene epoxidation with O_2 and H_2. Appl. Catal. B 95, 430–438.

Hughes, M.D., Xu, Y.-J., Jenkins, P., McMorn, P., Landon, P., Enache, D.I., Carley, A.F., Attard, G.A., Hutchings, G.J., King, F., Stitt, E.H., Johnston, P., Griffin, K., Kiely, C.J., 2005. Tunable gold catalysts for selective hydrocarbon oxidation under mild conditions. Nature 437, 1132–1135.

Janssen, J.A.M., 1989a. The elimination of fast variables in complex chemical reactions. II. Mesoscopic level (reducible case). J. Stat. Phys. 57, 171–185.

Janssen, J.A.M., 1989b. The elimination of fast variables in complex chemical reactions. III. Mesoscopic level (irreducible case). J. Stat. Phys. 57, 187–198.

Jones, G.S., Mavrikakis, M., Barteau, M.A., Vohs, J.M., 1998. First synthesis, experimental and theoretical vibrational spectra of an oxametallacycle on a metal surface. J. Am. Chem. Soc. 120, 3196–3204.

Joshi, A.M., Delgass, W.N., Thomson, K.T., 2006. Partial oxidation of propylene to propylene oxide over a neutral gold trimer in the gas phase: a density functional theory study. J. Phys. Chem. B 110, 2572–2581.

Joshi, A.M., Delgass, W.N., Thomson, K.T., 2007a. Investigation of gold−silver, gold−copper, and gold−palladium dimers and trimers for hydrogen peroxide formation from H_2 and O_2. J. Phys. Chem. C 111, 7384–7395.

Joshi, A.M., Delgass, W.N., Thomson, K.T., 2007b. Mechanistic implications of Au_n/Ti-lattice proximity for propylene epoxidation. J. Phys. Chem. C 111, 7841–7844.

Kettemann, F., Witte, S., Birnbaum, A., Paul, B., Clavel, G., Pinna, N., Rademann, K., Kraehnert, R., Polte, J., 2017. Unifying concepts in room-temperature CO oxidation with gold catalysts. ACS Catal. 7, 8247–8254.

Kim, J., Chung, Y.-M., Kang, S.-M., Choi, C.-H., Kim, B.-Y., Kwon, Y.-T., Kim, T.J., Oh, S.-H., Lee, C.-S., 2012. Palladium nanocatalysts immobilized on functionalized resin for the direct synthesis of hydrogen peroxide from hydrogen and oxygen. ACS Catal. 2, 1042–1048.

Landon, P., Collier, P.J., Carley, A.F., Chadwick, D., Papworth, A.J., Burrows, A., Kiely, C.J., Hutchings, G.J., 2003. Direct synthesis of hydrogen peroxide from H_2 and O_2 using Pd and Au catalysts. PCCP 5, 1917–1923.

Landon, P., Collier, P.J., Papworth, A.J., Kiely, C.J., Hutchings, G.J., 2002. Direct formation of hydrogen peroxide from H_2/O_2 using a gold catalyst. Chem. Commun., 2058–2059

Lee, W.-S., Lai, L.-C., Cem Akatay, M., Stach, E.A., Ribeiro, F.H., Delgass, W.N., 2012. Probing the gold active sites in Au/TS-1 for gas-phase epoxidation of propylene in the presence of hydrogen and oxygen. J. Catal. 296, 31–42.

Linic, S., Barteau, M.A., 2002. Formation of a stable surface oxametallacycle that produces ethylene oxide. J. Am. Chem. Soc. 124, 310–317.

Linic, S., Medlin, J.W., Barteau, M.A., 2002. Synthesis of oxametallacycles from 2-iodoethanol on Ag(111) and the structure dependence of their reactivity. Langmuir 18, 5197–5204.

Liu, J.-C., Tang, Y., Chang, C.-R., Wang, Y.-G., Li, J., 2016. Mechanistic insights into propene epoxidation with O_2–H_2O mixture on Au_7/α-Al_2O_3: a hydroproxyl pathway from ab initio molecular dynamics simulations. ACS Catal. 6, 2525–2535.

Liu, X., Friend, C.M., 2010. Competing epoxidation and allylic hydrogen activation: trans-β-methylstyrene oxidation on Au(111). J. Phys. Chem. C 114, 5141–5147.

Lu, J., Behtash, S., Heyden, A., 2012. Theoretical investigation of the reaction mechanism of the decarboxylation and decarbonylation of propanoic acid on Pd (111) model surfaces. J. Phys. Chem. C 116, 14328–14341.

Lu, J., Zhang, X., Bravo-Suárez, J.J., Tsubota, S., Gaudet, J., Oyama, S.T., 2007. Kinetics of propylene epoxidation using H_2 and O_2 over a gold/mesoporous titanosilicate catalyst. Catal. Today 123, 189–197.

Lu, Z., Piernavieja-Hermida, M., Turner, C.H., Wu, Z., Lei, Y., 2018. Effects of TiO_2 in low temperature propylene epoxidation using gold catalysts. J. Phys. Chem. C 122, 1688–1698.

Masatake, H., Tetsuhiko, K., Hiroshi, S., Nobumasa, Y., 1987. Novel gold catalysts for the oxidation of carbon monoxide at a temperature far below 0 °C. Chem. Lett. 16, 405–408.

Mavrikakis, M., Doren, D.J., Barteau, M.A., 1998. Density functional theory calculations for simple oxametallacycles: trends across the periodic table. J. Phys. Chem. B 102, 394–399.

Mavrikakis, M., Stoltze, P., Nørskov, J.K., 2000. Making gold less noble. Catal. Lett. 64, 101–106.

McEntee, M., Tang, W., Neurock, M., Yates, J.T., 2015. Mechanistic insights into the catalytic oxidation of carboxylic acids on Au/TiO_2: partial oxidation of propionic and butyric acid to gold ketenylidene through unsaturated acids. ACS Catal. 5, 744–753.

Mei, D., Du, J., Neurock, M., 2010. First-principles-based kinetic Monte Carlo simulation of nitric oxide reduction over platinum nanoparticles under lean-burn conditions. Ind. Eng. Chem. Res. 49, 10364–10373.

Mei, D., Neurock, M., Smith, C.M., 2009. Hydrogenation of acetylene–ethylene mixtures over Pd and Pd–Ag alloys: First-principles-based kinetic Monte Carlo simulations. J. Catal. 268, 181–195.

Mei, D., Sheth, P.A., Neurock, M., Smith, C.M., 2006. First-principles-based kinetic Monte Carlo simulation of the selective hydrogenation of acetylene over Pd (111). J. Catal. 242, 1–15.

Moskaleva, L.V., 2016. Theoretical mechanistic insights into propylene epoxidation on Au-based catalysts: Surface O versus OOH as oxidizing agents. Catal. Today 278, 45–55.

Mul, G., Zwijnenburg, A., van der Linden, B., Makkee, M., Moulijn, J.A., 2001. Stability and selectivity of Au/TiO_2 and Au/TiO_2/SiO_2 catalysts in propene epoxidation: an in situ FT-IR study. J. Catal. 201, 128–137.

Nijhuis, T.A., Huizinga, B.J., Makkee, M., Moulijn, J.A., 1999. Direct epoxidation of propene using gold dispersed on TS-1 and other titanium-containing supports. Ind. Eng. Chem. Res. 38, 884–891.

Nijhuis, T.A., Makkee, M., Moulijn, J.A., Weckhuysen, B.M., 2006. The production of propene oxide: catalytic processes and recent developments. Ind. Eng. Chem. Res. 45, 3447–3459.

Nijhuis, T.A., Visser, T., Weckhuysen, B.M., 2005a. Mechanistic study into the direct epoxidation of propene over gold/titania catalysts. J. Phys. Chem. B 109, 19309–19319.

Nijhuis, T.A., Visser, T., Weckhuysen, B.M., 2005b. The role of gold in gold–titania epoxidation catalysts. Angew. Chem. Int. Ed. 44, 1115–1118.

Ojeda, M., Iglesia, E., 2009. Catalytic epoxidation of propene with H_2O–O_2 reactants on Au/TiO_2. Chem. Commun., 352–354

Okumura, M., Fujitani, T., Huang, J., Ishida, T., 2015. A career in catalysis: Masatake Haruta. ACS Catal. 5, 4699–4707.

Olivera, P.P., Patrito, E.M., Sellers, H., 1994. Hydrogen peroxide synthesis over metallic catalysts. Surf. Sci. 313, 25–40.

Özbek, M.O., van Santen, R.A., 2013. The mechanism of ethylene epoxidation catalysis. Catal. Lett. 143, 131–141.

Panayotov, D., McEntee, M., Burrows, S., Driscoll, D., Tang, W., Neurock, M., Morris, J., 2016. Infrared studies of propene and propene oxide adsorption on nanoparticulate Au/TiO_2. Surf. Sci. 652, 172–182.

Park, S., Choi, J.H., Kim, T.J., Chung, Y.-M., Oh, S.-H., Song, I.K., 2012a. Direct synthesis of hydrogen peroxide from hydrogen and oxygen over Pd/$Cs_XH_{3-X}PW_{12}O_{40}$/MCF (X=1.7, 2.0, 2.2, 2.5, and 2.7) catalysts. J. Mol. Catal. A: Chem. 353–354, 37–43.

Park, S., Jung, J.C., Seo, J.G., Kim, T.J., Chung, Y.-M., Oh, S.-H., Song, I.K., 2009a. Direct synthesis of hydrogen peroxide from hydrogen and oxygen over palladium catalysts supported on SO_3H-functionalized SiO_2 and TiO_2. Catal. Lett. 130, 604–607.

Park, S., Lee, J., Song, J.H., Kim, T.J., Chung, Y.-M., Oh, S.-H., Song, I.K., 2012b. Direct synthesis of hydrogen peroxide from hydrogen and oxygen over Pd/HZSM-5 catalysts: Effect of Brönsted acidity. J. Mol. Catal. A: Chem. 363–364, 230–236.

Park, S., Seo, J.G., Jung, J.C., Baeck, S.-H., Kim, T.J., Chung, Y.-M., Oh, S.-H., Song, I.K., 2009b. Direct synthesis of hydrogen peroxide from hydrogen and oxygen over palladium catalysts supported on TiO_2–ZrO_2 mixed metal oxides. Catal. Commun. 10, 1762–1765.

Perez Ferrandez, D.M., Herguedas Fernandez, I., Teley, M.P.G., de Croon, M.H.J.M., Schouten, J.C., Nijhuis, T.A., 2015. Kinetic study of the selective oxidation of propene with O_2 over Au–Ti catalysts in the presence of water. J. Catal. 330, 396–405.

Pulido, A., Boronat, M., Corma, A., 2012. Propene epoxidation with $H_2/H_2O/O_2$ mixtures over gold atoms supported on defective graphene: a theoretical study. J. Phys. Chem. C 116, 19355–19362.

Rao, C.V., Arkin, A.P., 2003. Stochastic chemical kinetics and the quasi-steady-state assumption: application to the Gillespie algorithm. J. Chem. Phys. 118, 4999–5010.

Rodriguez, J.A., Liu, P., Hrbek, J., Evans, J., Pérez, M., 2007. Water gas shift reaction on Cu and Au nanoparticles supported on CeO_2(111) and ZnO(000): intrinsic activity and importance of support interactions. Angew. Chem. Int. Ed. 46, 1329–1332.

Samant, A., Vlachos, D.G., 2005. Overcoming stiffness in stochastic simulation stemming from partial equilibrium: A multiscale Monte Carlo algorithm. J. Chem. Phys. 123, 144114.

Siler, C.G.F., Cremer, T., Rodriguez-Reyes, J.C.F., Friend, C.M., Madix, R.J., 2014. Switching selectivity in oxidation reactions on gold: the mechanism of C-C vs C–H bond activation in the acetate intermediate on Au(111). ACS Catal. 4, 3281–3288.

Sivadinarayana, C., Choudhary, T.V., Daemen, L.L., Eckert, J., Goodman, D.W., 2004. The nature of the surface species formed on Au/TiO_2 during the reaction of H_2 and O_2: an inelastic neutron scattering study. J. Am. Chem. Soc. 126, 38–39.

Stangland, E.E., Stavens, K.B., Andres, R.P., Delgass, W.N., 2000. Characterization of gold–titania catalysts via oxidation of propylene to propylene oxide. J. Catal. 191, 332–347.

Taylor, B., Lauterbach, J., Blau, G.E., Delgass, W.N., 2006. Reaction kinetic analysis of the gas-phase epoxidation of propylene over Au/TS-1. J. Catal. 242, 142–152.

Torres, D., Lopez, N., Illas, F., Lambert, R.M., 2005. Why copper is intrinsically more selective than silver in alkene epoxidation: ethylene oxidation on Cu(111) versus Ag(111). J. Am. Chem. Soc. 127, 10774–10775.

Torres, D., Lopez, N., Illas, F., Lambert, R.M., 2007. Low-basicity oxygen atoms: a key in the search for propylene epoxidation catalysts. Angew. Chem. Int. Ed. 46, 2055–2058.

Turner, C.H., Ji, J., Lu, Z., Lei, Y., 2017. Analysis of the propylene epoxidation mechanism on supported gold nanoparticles. Chem. Eng. Sci. 174, 229–237.

Turner, C.H., Lei, Y., Bao, Y., 2016. Modeling the atomistic growth behavior of gold nanoparticles in solution. Nanoscale 8, 9354–9365.

Turner, M., Golovko, V.B., Vaughan, O.P.H., Abdulkin, P., Berenguer-Murcia, A., Tikhov, M.S., Johnson, B.F.G., Lambert, R.M., 2008. Selective oxidation with dioxygen by gold nanoparticle catalysts derived from 55-atom clusters. Nature 454, 981–983.

Uphade, B.S., Akita, T., Nakamura, T., Haruta, M., 2002. Vapor-phase epoxidation of propene using H_2 and O_2 over Au/Ti–MCM-48. J. Catal. 209, 331–340.

Valden, M., Lai, X., Goodman, D.W., 1998. Onset of catalytic activity of gold clusters on titania with the appearance of nonmetallic properties. Science 281, 1647–1650.

Wells, D.H., Delgass, W.N., Thomson, K.T., 2004a. Evidence of defect-promoted reactivity for epoxidation of propylene in titanosilicate (TS-1) catalysts: a DFT study. J. Am. Chem. Soc. 126, 2956–2962.

Wells, D.H., Delgass, W.N., Thomson, K.T., 2004b. Formation of hydrogen peroxide from H_2 and O_2 over a neutral gold trimer: a DFT study. J. Catal. 225, 69–77.

Xu, Y., Mavrikakis, M., 2003. Adsorption and dissociation of O_2 on gold surfaces: effect of steps and strain. J. Phys. Chem. B 107, 9298–9307.

Yap, N., Andres, R.P., Delgass, W.N., 2004. Reactivity and stability of Au in and on TS-1 for epoxidation of propylene with H_2 and O_2. J. Catal. 226, 156–170.

Yoon, B., Häkkinen, H., Landman, U., Wörz, A.S., Antonietti, J.-M., Abbet, S., Judai, K., Heiz, U., 2005. Charging effects on bonding and catalyzed oxidation of CO on Au_8 clusters on MgO. Science 307, 403–407.

Zheng, Z., Stephens, R.M., Braatz, R.D., Alkire, R.C., Petzold, L.R., 2008. A hybrid multiscale kinetic Monte Carlo method for simulation of copper electrodeposition. J. Comput. Phys. 227, 5184–5199.

Zwijnenburg, A., Makkee, M., Moulijn, J.A., 2004. Increasing the low propene epoxidation product yield of gold/titania-based catalysts. Appl. Catal., A 270, 49–56.